

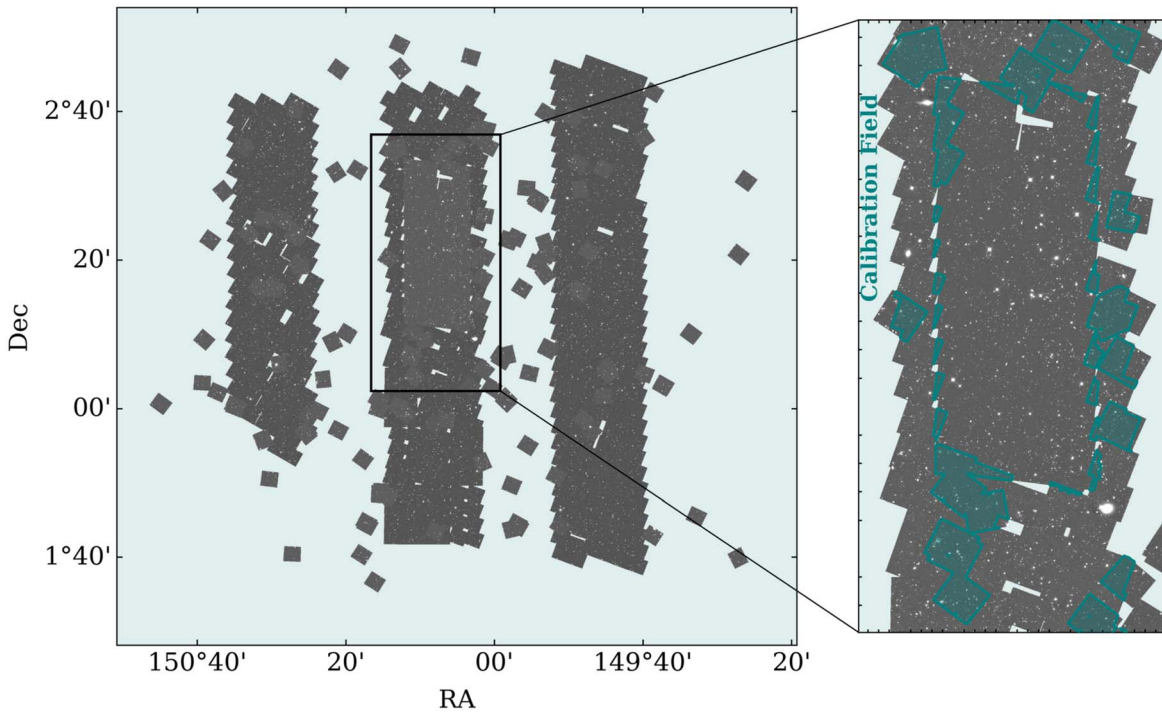


Diagnosing DASH: A Catalog of Structural Properties for the COSMOS-DASH Survey

Sam E. Cutler¹, Katherine E. Whitaker^{1,2}, Lamiya A. Mowla³, Gabriel B. Brammer^{2,4}, Arjen van der Wel⁵, Danilo Marchesini⁶, Pieter G. van Dokkum⁷, Ivelina G. Momcheva⁸, Mimi Song¹, Mohammad Akhshik⁹, Erica J. Nelson

et al. 2012; Shibuya et al. 2015; Holwerda et al. 2015; Nelson et al. 2016; Dimauro et al. 2018, 2019; Nedkova et al. 2021). To name a few, this data yields clear evidence for inside out disk growth (Wuyts et al. 2012; Nelson et al. 2016), establishes correlations between quiescence and galaxy morphology (Bell et al. 2012), and uncovers the striking diversity of morphologies among massive galaxies at high redshift (van Dokkum et al. 2011). Structural measurements from van der Wel et al. (2012) are also fundamental to establishing significant correlations between the surface mass densities of star-forming and quiescent galaxies (e.g., Whitaker et al. 2017); these results inspired astronomers to coin a new term, the structural main sequence, that hypothesizes a universal evolution track of compaction among star-forming galaxies (Barro et al. 2013, 2017).

Combining procedures and imaging utilized in the CANDELS morphological catalogs by van der Wel et al.



Due to the limited spatial resolution of ground-based UVISTA observations (K-band FWHM $\sim 0''.8$ versus HST F160W FWHM $\sim 0''.151$), some sources cataloged as a single object in UVISTA will be deblended into two or more objects in COSMOS-DASH. Of the 51,586 galaxies in DASH, 2,345 are split into pairs or triplets when searching within the UVISTA FWHM. Adapting from Mowla et al. (2019b), for each deblended UVISTA ID we compute F160W total fluxes using GALFIT (Peng et al. 2002, 2010a), making sure to mask the other deblended objects. The brightest galaxy is retained, with the stellar mass weighted by its flux relative to the total flux of all of the blended components:

$$M_{*,i} = M_{*,\text{tot}} \times \frac{F_i}{F_{\text{tot}}}, \quad (1)$$

where $M_{*,\text{tot}}$ is the total mass of the blended object from the UVISTA catalog, F_i is the model flux of the brightest component and F_{tot} is the total summed fluxes of all the components. The mass corrections are provided in the catalog of this sample (see Section 4).

The deblending status of the galaxies in the sample is indicated with a blending flag. HST-selected galaxies that have no close pairs are given a flag of 0, and are labeled “not blended”. Galaxies whose components can be properly deblended and fit with GALFIT are flagged with 1, indicating they are “deblended”. Deblended galaxies whose $U - V$ and $V - J$ colors do not change likely have robust masses and morphologies, but significant color changes may suggest that stellar masses and/or photometric redshifts are incorrect. Galaxies that remain “blended,” meaning the deblending procedure failed, are given a flag of 2. Lastly, a flag of 4 is given to galaxies that are in the UVISTA catalogs, but have “no coverage” with COSMOS-DASH. This flag value is chosen to match with the “no coverage” GALFIT flag (see Section 3.1). Since later analyses in this work use rest-frame colors from UV

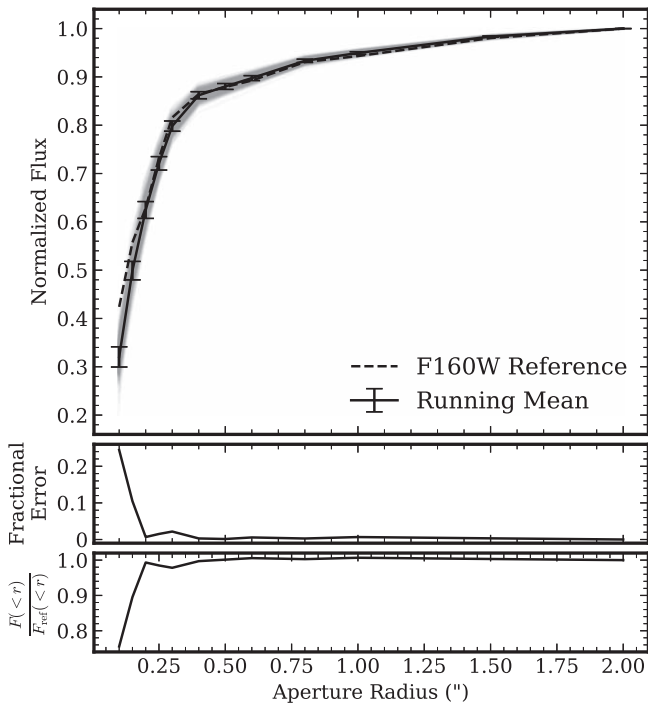


Figure 2. Normalized curve of growth for PSFs determined at positions of calibration field galaxies. The gray transparent lines are the growth curves for each of the 483 galaxies in the calibration field. The solid black line shows the running mean of the individual growth curves, with error from the standard deviation of the individual growth curves. The dashed line shows the F160W reference growth curve. The reference flux and each individual growth curve is normalized to unity at 2". The middle panel shows the fractional error in the growth curve, and the bottom panel shows the ratio between the reference curve and the running mean.

fit without problems are assigned a flag of zero and are deemed “good” fits. “Suspicious” fits, sources whose GALFIT magnitudes deviate by more than 3σ (as determined in Section 3.5) from the expected magnitude, are given a flag of 1. The expected magnitudes are measured in Section 3.3 and are corrected for previously noted systematic offsets between GALFIT and SExtractor magnitudes, which range from roughly 0.1 dex at bright magnitudes to 0.3 dex at faint magnitudes (see e.g., Häussler et al. 2007; van der Wel et al. 2012). Galaxies that have a best-fit parameter at the constraint limits are considered “bad” and flagged with a value of 2. When GALFIT fails to converge at all, the fit is marked with a flag of 3, and we indicate the fit as “failed”. Moreover, galaxies that have a negative aperture flux are also given a flag of 3, as the signal-to-noise ratio (S/N) is crucial in estimating parameter errors (see Section 3.5). These galaxies account for only 0.5% of all 51,586 galaxies with coverage. Lastly, we assign a flag of 4, differing from van der Wel et al. (2012), to galaxies in UVISTA that are not covered by COSMOS-DASH imaging. Though analysis is not possible for galaxies without COSMOS-DASH coverage, we still include these objects in order to present a complete list of IDs in the catalog (see Section 4). In total, 39.5% of galaxies with coverage are “suspicious,” 12.7% are “bad,” and 0.5% are “failed.” “Suspicious” galaxies are not necessarily poorly fit or reporting inaccurate magnitudes. In most cases, these are galaxies with very small GALFIT magnitude errors, so there is less of a deviation required for a flag to be applied. On average, “good” galaxies had a magnitude error that was 70% larger than “suspicious” galaxies.

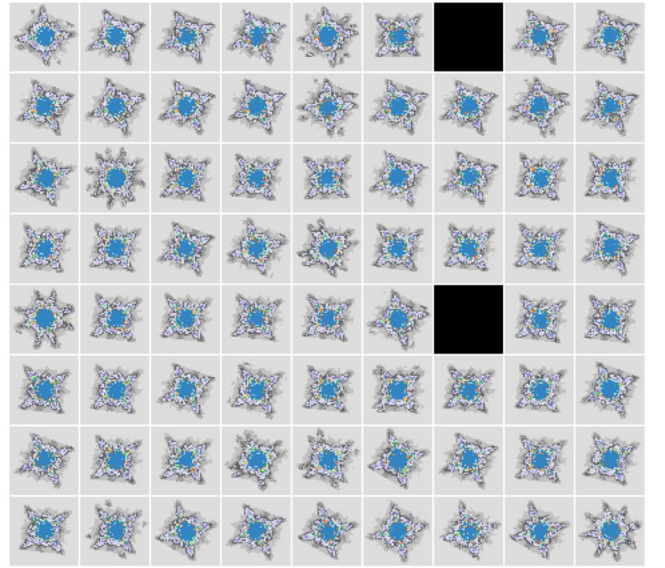


Figure 3. Grid of all 72 empirical PSFs for the COSMOS-DASH mosaic. Empirical PSFs are inserted in the frame of each exposure that covers a given position within the mosaic, and the PSFs are then drizzled with the same parameters as the science exposures. Black squares show regions where there is no PSF available because there are no dithering parameters.

3.2. PSF Models

We obtain PSFs for COSMOS-DASH using Grizli²⁰ to shift and drizzle HST empirical PSFs (Anderson 2016) to (1) the location of every source, or (2) a coarser grid of positions throughout the mosaic when running GALFIT. Using the Grizli determined PSFs for all 483 galaxies in the COSMOS-DASH calibration field, we obtain growth curves for each galaxy (Figure 2). The running mean and the standard deviation of the 483 individual growth curves is also calculated at each aperture size. We compare the running mean to the HST F160W reference curve and determine that there is no significant difference for aperture radii $\gtrsim 0''.25$. Similarly, scatter in the position dependent PSFs is also negligible for a given aperture size. Moreover, there is no significant difference in structural measurements between galaxies fit with position-dependent PSFs and those fit with PSFs determined over a larger area of the mosaic, even at $z > 2$. This suggests that further corrections to the PSF at each individual location in the mosaic are unnecessary.

Due to the time it takes to determine each individual PSF and the minimal effect of individual position dependent PSFs, we alternatively opt for a set of empirical PSFs evaluated on a coarse grid across the mosaic. The 72 PSFs for the COSMOS-DASH mosaic are shown in Figure 3. These are empirical PSFs that are altered to match the mosaic pixel scale and the dither grid at each position. In regions where there are no dithering parameters (due to the image being empty), the PSFs are also empty. These PSFs have an average FWHM of $0''.2$, compared to $0''.18$ in CANDELS. For each galaxy, the closest PSF by R.A. and decl. is chosen, excluding empty PSFs. Further corrections (such as 2D interpolations) are not done due to the added computational time and negligible change in fit quality. This PSF is then used by GALFIT when fitting a

3.3. Photometry and Noise Properties

We compute the flux density of all 51,586 galaxies within a $0''.7$ diameter aperture using SExtractor. This aperture size is chosen to maximize the S/N of HST observations (Skelton et al. 2014). The Kron radius and Kron radius flux (AUTO flux) are also computed by SExtractor. The aperture flux is scaled to a total flux by correcting first to the flux within the Kron radius. We then interpolate the value of the growth curve (normalized to unity at $2''$) at the Kron radius and multiply the inverse of this value to obtain the total flux. If the AUTO flux is less than the aperture flux or the Kron radius is greater than $2''$, then that scaling is kept at one following Skelton et al. (2014).

Photometric errors are estimated using an empty apertures approach (e.g., Whitaker et al. 2011; Skelton et al. 2014). For a diameter in the range of $0''.2$ – $2''$, 2000 circular apertures are placed in empty regions of the noise-equalized, background-subtracted image. Apertures that overlap with objects based on the segmentation map or regions outside of the image are moved to different random coordinates until satisfactory. The distribution of the summed fluxes obtained for 6 aperture diameters ranging from $0''.5$ to $2''$ is shown in Figure 4 (top). The shifts in the Gaussian means indicate a small, per-pixel background, as shown in Figure 4 (bottom), which gets larger in magnitude as more pixels are included in the aperture. The figure also demonstrates that the widths of the best-fit Gaussians increase with larger aperture sizes, which implies an increase in standard deviation with linear aperture size $N = \sqrt{A}$, where A is the area of the aperture. This relation is modeled by a power law of the form

$$\sigma_{\text{nmad}} = \sigma_1 \alpha N^\beta, \quad (3)$$

where σ_1 is the standard deviation of the pixels of background pixels, α is the normalization, and β is the power-law index, which falls between 1 and 2 (see Whitaker et al. 2011). A power-law index of 1 indicates uncorrelated noise, and a power-law index of 2 indicates perfectly correlated noise. The combined COSMOS-DASH mosaic (outside the nominal CANDELS footprint) contains shallower DASH-mode pointings alongside deeper standard HST observations (from archival imaging); we fit a separate power law for DASH- and standard-depth observations. The distinction in depth is determined from the weight maps, with a boundary set at a weight of 100, corresponding to a 5σ depth of 26.7 ABmag (as calculated directly from the weight map). The resulting fit is shown in Figure 5. The standard-depth (CANDELS) imaging shows a higher level of correlation due to the finer spatial grid (when compared to DASH). To convert this standard deviation into a physical error, the noise equalization factor (\sqrt{w} , where w is the weight) must be divided out.

To find the photometric error of each source, empty aperture error at the Kron radius is computed and added in quadrature to Poisson noise as follows:

$$\sigma_{\text{Kron}}^2 = \left(\frac{\sigma_1 \alpha (\pi R_{\text{Kron}}^2)^{\frac{\beta}{2}}}{\sqrt{w}} \right)^2 + \frac{F_{\text{AUTO}}}{g}, \quad (4)$$

where w is the weight of the source, F_{AUTO} is the Kron radius flux of the source, and g is the effective gain (detector gain times exposure time) of the data. This is then scaled to a total error using the growth curve in the same way as the flux.

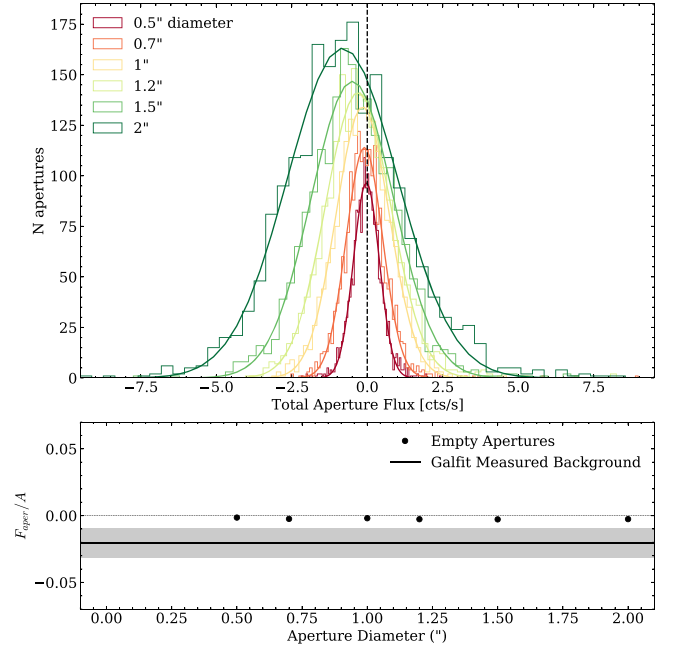


Figure 4. Empty aperture photometry on the background COSMOS-DASH calibration field. The top panel shows histograms of the summed flux in different aperture sizes from empty regions in the image. The solid lines are the best-fit Gaussians to these histograms. The bottom

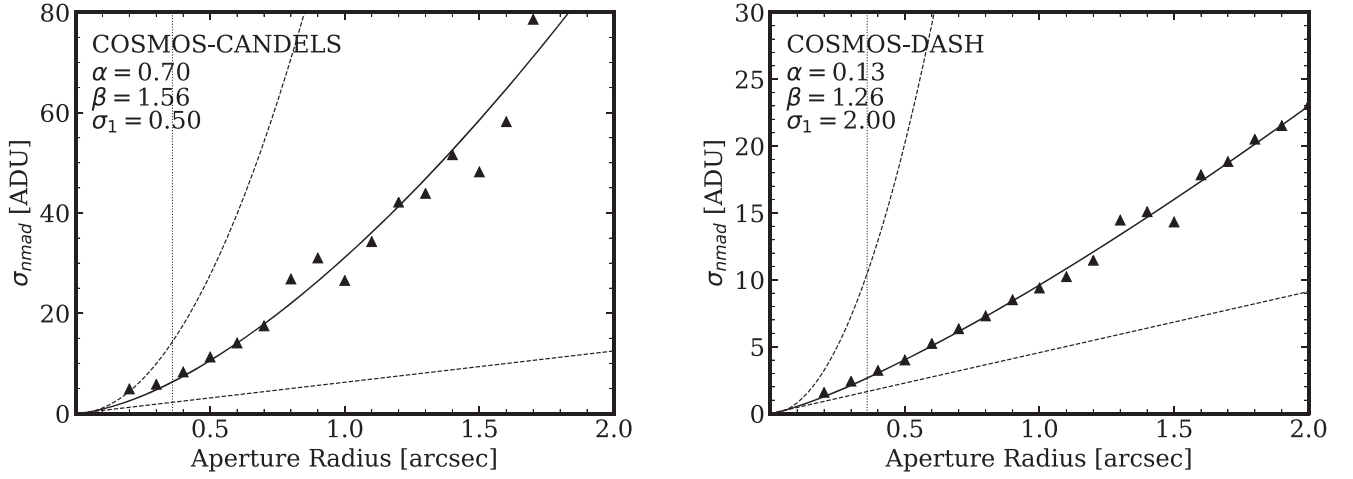


Figure 5. Empty aperture errors for CANDELS-only (left) and DASH-only (right) reductions of the COSMOS-DASH mosaic. The measured best-fit Gaussian width to the flux distribution of 2000 apertures are indicated with triangles for a range of aperture sizes. The solid line indicates the best-fit power law given by Equation (3). Dashed lines show uncorrelated and perfectly correlated noise below and above the best-fit line, respectively. The dotted line shows the PSF FWHM. The best-fit power-law parameters for each reduction are shown in the top left of each figure.

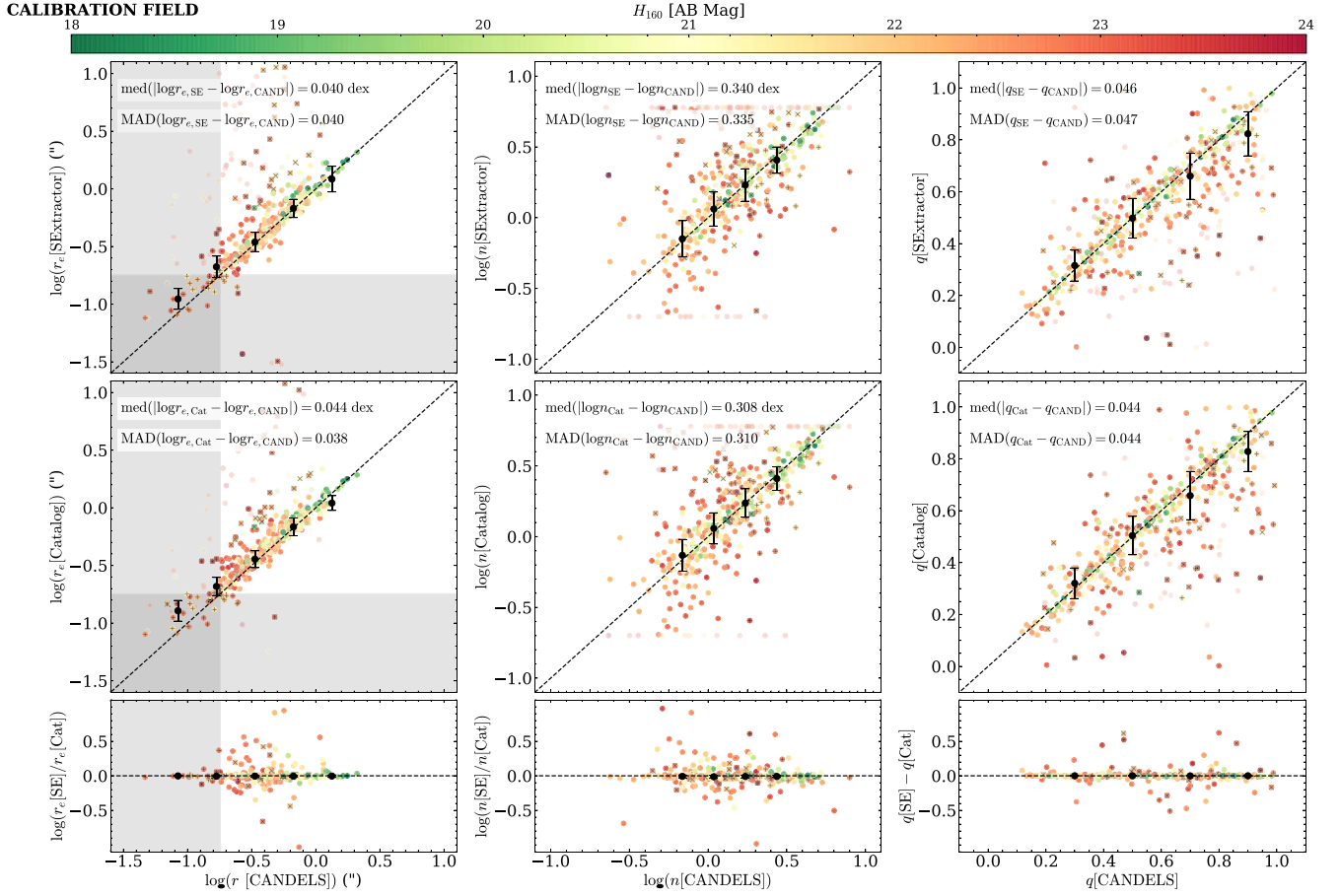


Figure 6. Scatter in the best-fit Sérsic parameters obtained using a deep-detection (Catalog) segmentation map is slightly smaller than with a DASH-depth (SEExtractor) segmentation map. The top and middle rows show the effective radii, Sérsic indices, and axis ratios of the best-fit Sérsic models determined with the DASH-depth segmentation map (top) and with the catalog segmentation map (middle), respectively, compared to those from CANDELS/3DHST (van der Wel et al. 2012). Transparent points are those with `flag=2` parameter values (see Section 3.1). The bottom row shows the difference in the parameters when measured both with and without fitting background. The large black points are the running median in each bin, with errorbars showing the scatter determined by the median absolute deviation (MAD) of the bin. The color scale indicates the H_{160} magnitude of the source in AB magnitudes. Points with a black x are those that are greater than 0.3 dex from the one-to-one line in radius. The gray shaded region shows radii less than the PSF FWHM and points with a black + are sources whose best-fit radius falls in this region. The median and MAD of the offset between parameters derived with the two segmentation maps and CANDELS is shown in each panel of the top and middle row.

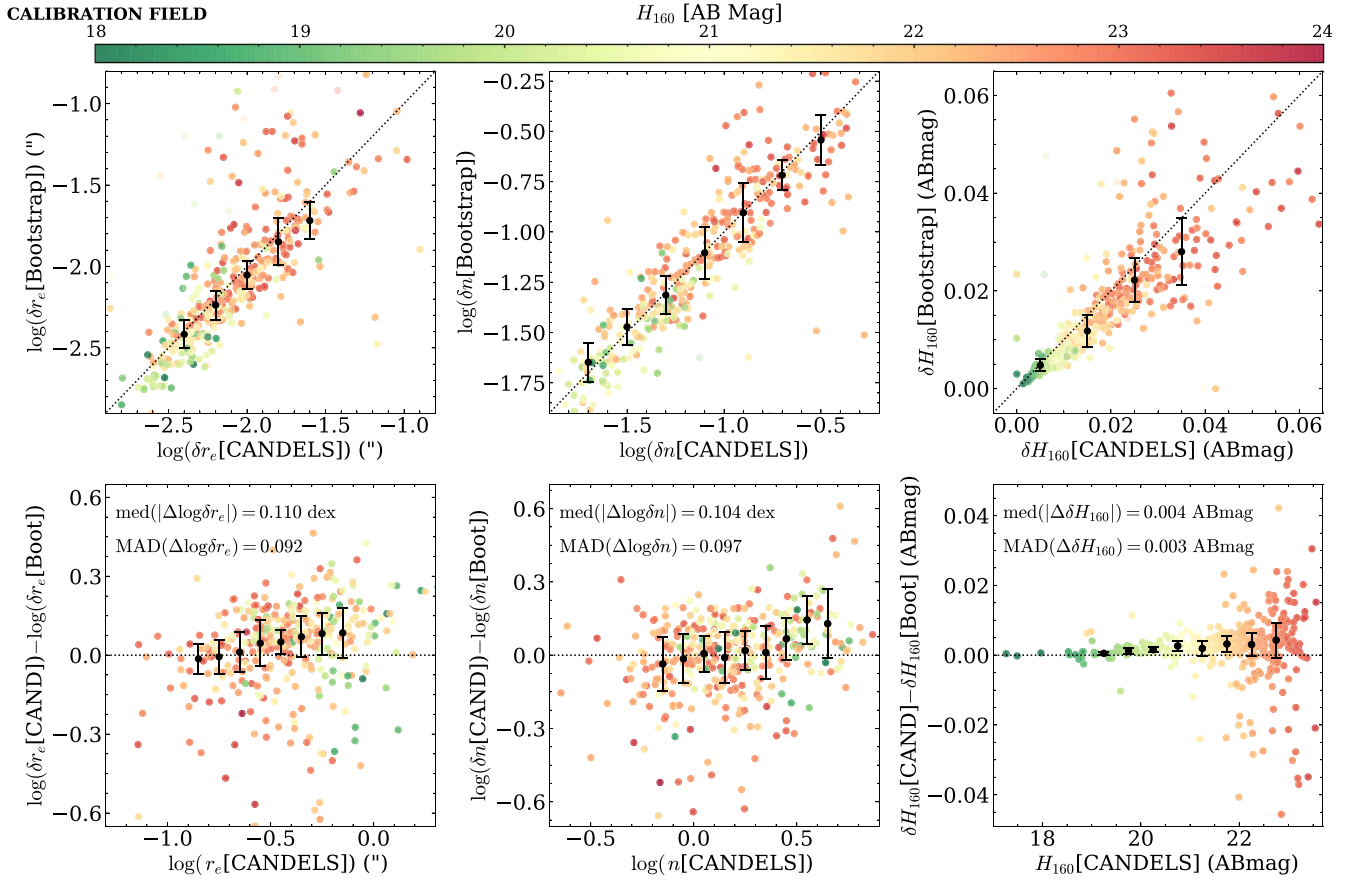


Figure 7. GALFIT parameter errors of calibration field galaxies derived from bootstrapping are in agreement with errors the CANDELS/3D-HST catalog. The top row shows, from left to right, the bootstrapping error in effective radius, Sérsic index, and magnitude plotted against the same errors from the CANDELS/3D-HST. Bootstrapping is run on galaxies in the CANDELS-only reduction of the calibration field. The dashed line shows the one-to-one line. The bottom row shows the difference between the CANDELS/3D-HST and bootstrapping errors plotted against the CANDELS/3D-HST effective radius, Sérsic index, and magnitude. The running median in each panel is shown with black points, and error bars are determined with the median absolute deviation. The dashed line shows a difference of zero. The color scale indicates the AB magnitude of each galaxy, as reported in the COSMOS-DASH catalog. The median and MAD of the offset between bootstrapping and CANDELS errors are indicated in each of the bottom panels.

cutouts (Section 3.1), similar to Mowla et al. (2019b), and the resulting segmentation maps are used with GALFIT. We run the GALFIT pipeline on the 483 calibration field galaxies using both segmentation maps.

In Figure 6, we compare the measured morphologies of both scenarios. The first row compares parameters measured using the DASH-depth segmentation map to the morphologies of corresponding galaxies in the CANDELS/3D-HST morphological catalog. The second row makes a similar comparison showing parameters measured using the deep-detection (catalog) segmentation maps. Galaxies with a flag value ≥ 3 are excluded from the plot, and objects with a flag of 2 are indicated with higher transparency and excluded from the bottom row of the figure. For the comparison, CANDELS/3D-HST galaxies with flags ≥ 2 (see, van der Wel et al. 2012) are also excluded. Objects that deviate significantly in radius (more than 0.3 dex) from CANDELS/3D-HST are indicated with black x’s. If a source has a measured radius less than the PSF FWHM ($0''.18$), it is marked with a black “+”, as radius measurements may be unreliable below the FWHM.

On average, both scenarios have morphologies consistent with those from the CANDELS/3D-HST catalog. We observe a 22% larger scatter in the measured radii and an 11% larger scatter in Sérsic indices for fits obtained with the DASH-depth segmentation map. Given the factor of two decrease in standard

deviation when using the deeper-detection segmentation map, we adopt the deep-detection segmentation map for masking, as this best represents the full

CALIBRATION FIELD

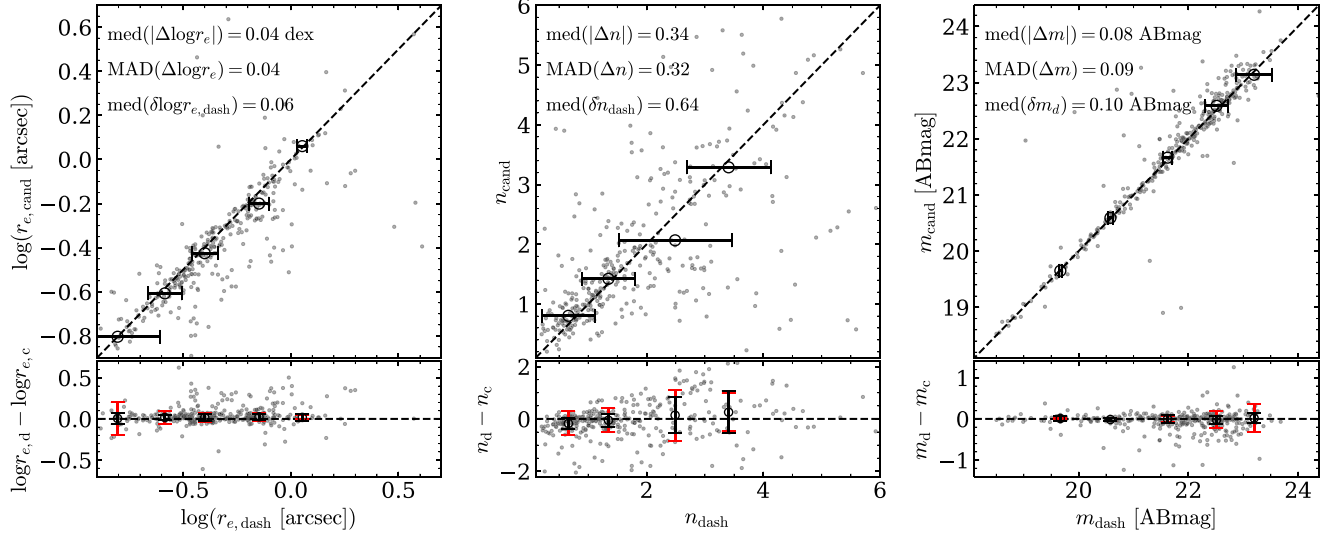


Figure 8. Size, Sérsic index, and magnitude comparison between calibration field galaxies in CANDELS/3D-HST and COSMOS-DASH, showing overall agreement between parameter values and random uncertainties consistent with scatter. In the top row, CANDELS/3D-HST parameters with GALFIT flags ≤ 1 (see van der Wel et al. 2012) are plotted against COSMOS-DASH parameters with GALFIT flags ≤ 1 . The running median and one-to-one line are shown with open circles and dashed lines, respectively. 1σ error bars show the average parameter error (from bootstrapping) in each running median bin. The bottom row shows the difference between CANDELS/3D-HST and COSMOS-DASH structural parameters plotted against the COSMOS-DASH parameters. The open circles again indicate the running median, while the dashed line shows a difference of zero. The black error bars are the median absolute deviation in the running median, while the red error bars show the average parameter error. The median and MAD of the difference in the structural parameters, as well as the average parameter error is also displayed in the top left of each panel.

the standard deviation is used as the error in the parameter measurement.

We test the bootstrapping method on the calibration field sample of galaxies using the CANDELS-only reduction. This allows us to make direct comparisons to the CANDELS/3D-HST morphological catalog errors, as these analyze the same sources at the same depth. In lieu of extrapolating to a single pixel, we adopt the empty aperture error within 3 pixels when running the bootstrapping simulations. We find this is consistent with CANDELS/3D-HST errors within 1σ . Figure 7 shows this comparison of CANDELS-only calibration field errors (from COSMOS-DASH) to CANDELS/3D-HST errors. Brighter sources have smaller errors, as these are more easily fit. There is also strong agreement between the photometric catalog magnitudes and the morphological catalog magnitudes (Figure 7, bottom right). Galaxies with smaller errors have less scatter around the one to one line than those with larger errors, which is expected as well. The parameter error difference is also less than 0.3 dex for most galaxies in both radius and Sérsic index and not significant in magnitude error for all but the faintest galaxies. This is confirmed by the median offsets between the errors, as well as the scatter in this offset (bottom panels, Figure 7).

We also directly compare the parameter values of calibration field galaxies in CANDE

the average of δ_i . We then divide δ_i by $(S/N)_i$ to properly normalize the parameter error. Log errors are converted to linear errors in the standard way, i.e., $\delta r = \ln(10) r \delta \log r$, and these errors are given in the morphological catalog. The relative errors of the full DASH sample are shown in Figure 9 compared to the corresponding GALFIT magnitudes.

3.6. Parameter Limits

Fainter and more noisy sources are expected to yield less robust structural diagnostics than bright, high-S/N galaxies. Thus, we can directly relate the depth of the data to the magnitude limit at which morphologies become unreliable. We measure the depth of the entire COSMOS-DASH mosaic (Figure 1) using empty apertures on the noise-equalized image (see Section 3.3). We separately place 2000 apertures in empty regions of DASH and CANDELS depth areas of the full mosaic. The width of the best-fit Gaussians for both aperture flux distributions is computed and used with the weight map to find a 5σ depth ($m_{5\sigma}$).

For CANDELS depth data ($m_{5\sigma} \sim 26.5$), galaxies brighter than $H_{F160W} \sim 24.5(23.5)$ had average fractional errors of 20% or lower for the parameters m , r_e , and q (n) (see also van der Wel et al. 2012). We find similar values for the CANDELS/3D-HST morphological catalog (24.9 and 23.7, respectively) using a 3σ clipped running mean. A similar analysis is done on the 51,586 DASH galaxies, shown in Figure 9. Fractional errors for both effective radius and Sérsic index are computed using the errors derived in Section 3.5 and the best-fit parameters from GALFIT (3.1). We compute the 5σ depth of each object and separate each galaxy in to 0.25 AB magnitude bins based on the depth of the image at their location. The fractional errors are plotted against the GALFIT best-fit magnitudes and color-scaled by the total S/N (i.e., the aperture S/N scaled to total using the curve of growth). A running mean over the respective GALFIT magnitudes is computed for each depth bin with outliers $> 3\sigma$ clipped (solid line in Figure 9). We interpolate the running mean to find the magnitude at which it equals a fractional error of 0.2 (marked with a dashed-dotted line in Figure 9) and quote that magnitude in the top left of each panel.

These values are then plotted against the corresponding 5σ depth in Figure 10 (solid points), along with the limits from CANDELS/3D-HST (open points). We separate the limits into two regimes, shown with a dotted line in Figure 10: $m_{5\sigma} < 24.5$, where the parameter limit is constant with changing depth; and $m_{5\sigma} > 24.5$, where there is a linear relationship between depth and magnitude limit. For the former, we measure the mean parameter limit for all bins with $m_{5\sigma} < 24.5$ and use this as the constant limit for this regime.²² For $m_{5\sigma} > 24.5$, ensuring continuity at $m_{5\sigma} = 24.5$, we fit a linear relation to the data. The resulting depth-parameter limits are

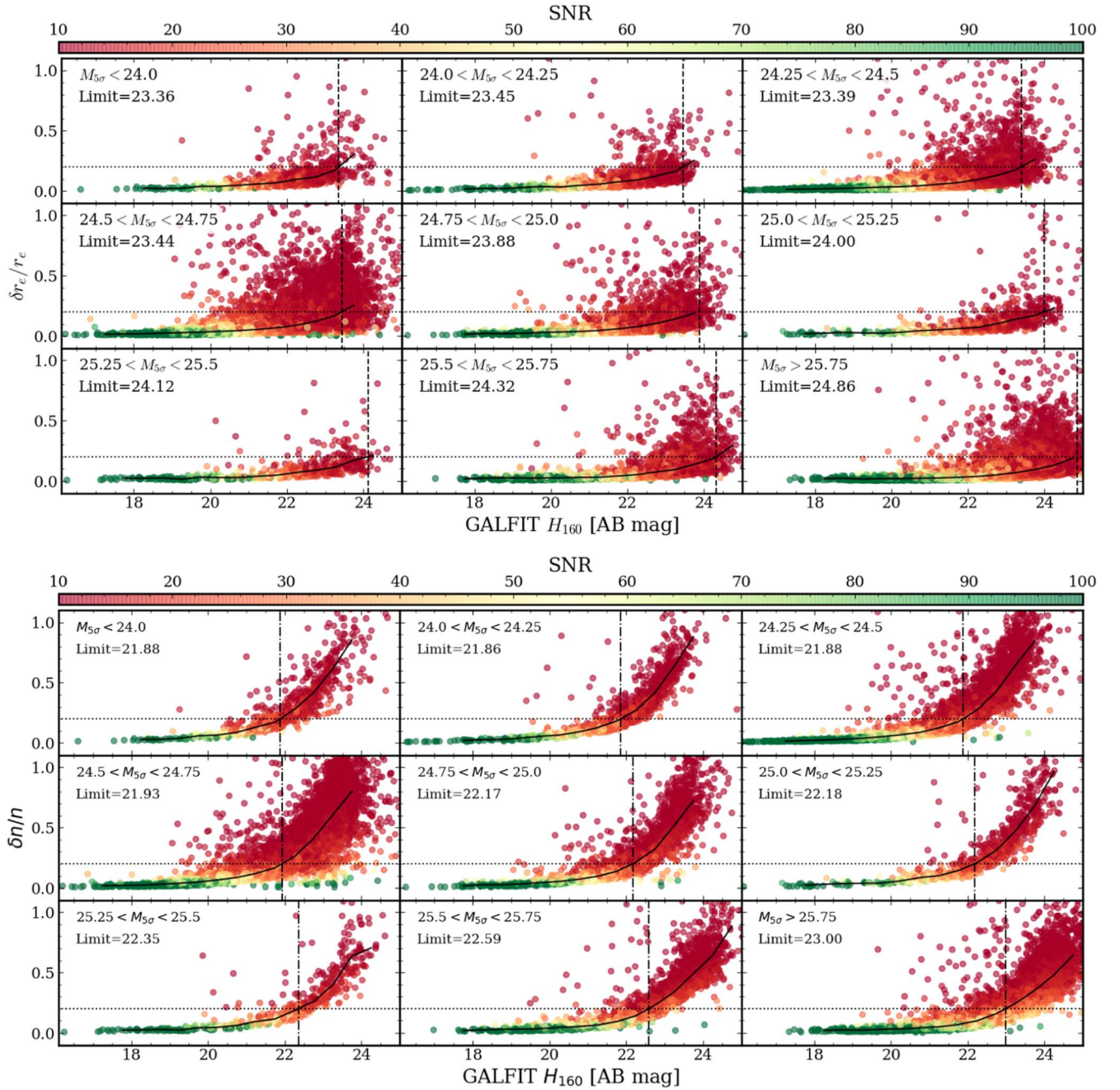


Figure 9. Evolution of relative uncertainty in effective radius (top) and Sérsic index (bottom) with increasing depth, resulting in the parameter magnitude limits of Figure 10. For each depth bin ($m_{5\sigma}$) given in the top left of each panel, relative errors in effective radius and Sérsic index (Sections 3.1 and 3.5) are plotted against the best-fit GALFIT magnitude. A 3σ clipped running mean is shown with a solid line. A relative error of 20% is marked by a dotted line. The running median is linearly interpolated to find the magnitude where the fractional error reaches 20%. This value is indicated with a dashed vertical line and explicitly stated by the limit in the top left of each panel. The color bar shows the S/N of each galaxy as computed in Section 3.3.

morphologies are robust, as well as the overall utility of DASH observations, we make direct comparisons to a combined sample of morphologies from other studies. This sample is made up of independent size measurements of galaxies in both the COSMOS-DASH and CANDELS imaging. The bulk of this sample is comprised of a mass-limited galaxy sample selected from all five fields of the CANDELS survey (Koekemoer et al. 2011), adopting measurements from the 3D-HST morphological catalogs (van der Wel et al. 2014; hereafter referred to as vdW14). This is augmented by morphologies from COSMOS-DASH imaging for ultramassive

galaxies²³ ($\log(M_*/M_\odot) > 11.3$; Mowla et al. 2019b; hereafter referred to as M19). In the M19 sample, COSMOS-DASH morphologies are only measured at $z > 1.5$, resulting in a sample size of 203 galaxies. 18 of the galaxies in this sample are split into pairs, and 14 of those remain above the $\log(M_*/M_\odot) > 11.3$ cut. Stellar masses, redshifts, and rest-frame $U - V$ and $V - J$ colors are taken from the UVISTA and are assigned to COSMOS-DASH galaxies based on matching

²³ This high-mass sample is available at <https://archive.stsci.edu/hlsp/cosmos-dash>

Table 2
Summary of Morphological Catalog Contents

Column No.	Column Title	Description
1	ID	Object identifier from UVISTA catalogs of Muzzin et al. (2013b)
2,3	RA, DEC	Right ascension and decl. (J2000; decimal degrees)
4	flag	GALFIT flags (see Section 3.1); 0 = good, 1=suspicious, 2 = bad, 3 = failed, 4 = no coverage
5	use	General use flag (see Section 4); 1 = GALFIT flag < 2, $r_e > \text{FWHM}$
6	mag	GALFIT best-fit magnitude
7	dmag	Uncertainty in GALFIT magnitude (see Section 3.5)
8	re	GALFIT best-fit effective (half-light) radius in arcsec
9	dre	Uncertainty in GALFIT effective radius in arcsec
10	n	GALFIT best-fit Sérsic index
11	dn	Uncertainty in GALFIT Sérsic index
12	q	GALFIT best-fit axis ratio
13	dq	Uncertainty in GALFIT axis ratio
14	pa	GALFIT best-fit position angle
15	dpa	Uncertainty in GALFIT position angle
16	kron	Kron radius from SExtractor in arcsec
17	f_F160W_auto	F160W AUTO flux (SExtractor measured flux within Kron radius); zero-point=25
18	e_F160W_auto	Error in F160W AUTO flux; zero-point=25
19	f_F160W_tot	F160W total flux (scaled from AUTO flux); zero-point=25
20	e_F160W_tot	Error in F160W total flux (scaled from AUTO flux error); zero-point=25
21	snr	Total signal-to-noise ratio ($f_{\text{F160W_tot}}/e_{\text{F160W_tot}}$)
22,23	flag_limit_r, flag_limit_n	Parameter robustness flags (see Section 4); 0 = not robust, 1 = robust
24	flag_deb	Deblending flag (see Section 2.2); 0 = not blended, 1 = debbled, 2 = blended, 4 = no coverage
25	Mcorr	Mass correction for debbled galaxies (see Section 2.2)
26	5_sigma_depth	Total 5σ depth measured from COSMOS-DASH mosaic (see Section 3.6)
27	chi	GALFIT chi-squared
28	chi_nu	GALFIT chi-squared per degree of freedom

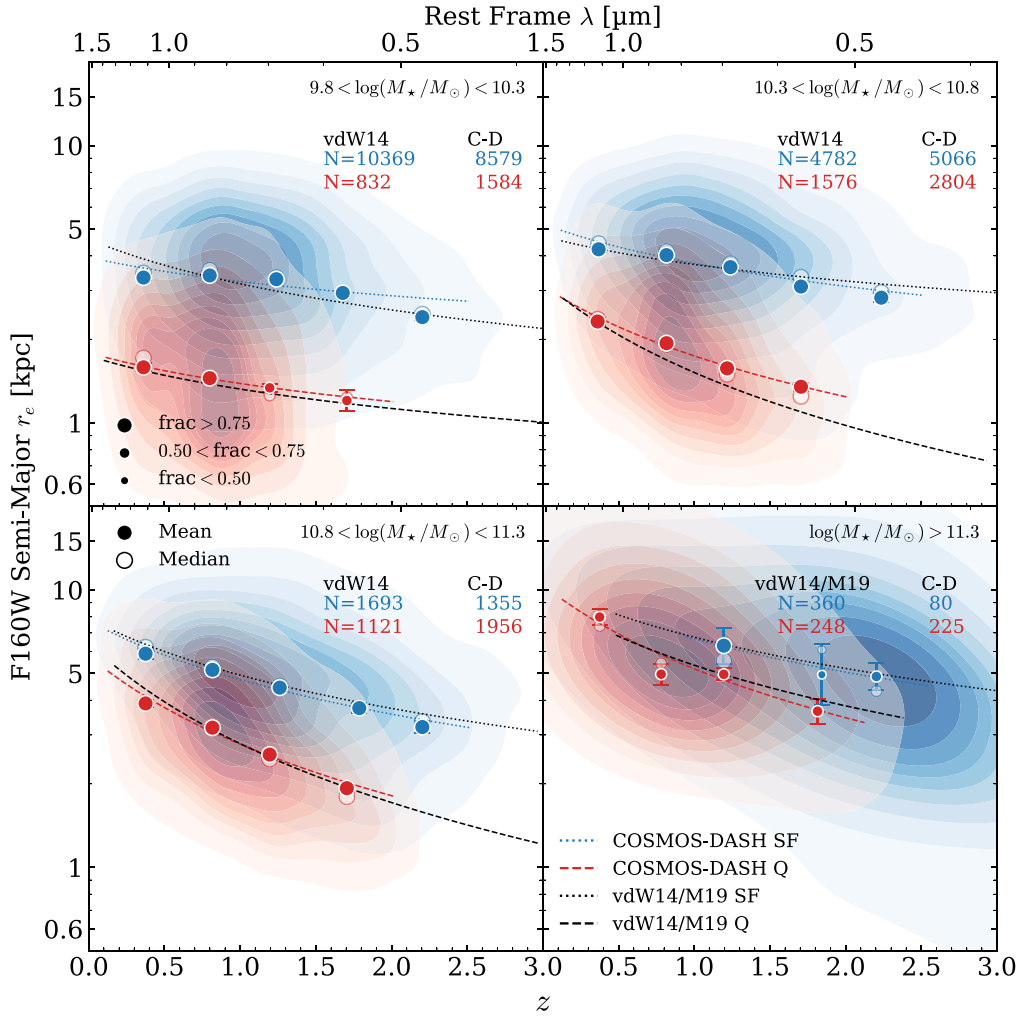


Figure 11. Evolution of quiescent (red) and star-forming (blue) galaxy size with redshift using morphologies from COSMOS-DASH is consistent with size-evolution trends from other studies. Galaxies are separated into mass bins (indicated in the top right of each panel). The distribution of quiescent and star-forming galaxies are shown with colored kernel density estimate contours. The running mean and median for both galaxy types are shown with solid and open points, respectively, and the size of the running mean/median points in each bin varies to reflect the fraction of DASH galaxies in that redshift-mass bin that have a GALFIT flag of 0 or 1 (see Section 3.1). Error bars are determined by the standard error of the mean within each redshift bin. The running means are fit with power laws, see Equation (10), and the corresponding best-fit line is shown as a dotted blue or dashed red line for star-forming and quiescent populations, respectively. The same fits are made to the combined sample of galaxies from 3D-HST (vdW14) and massive ($\log(M_*/M_\odot) > 11.3$) COSMOS-DASH morphologies (Mowla et al. 2019b) (M19). These are shown with black dotted and dashed lines for star-forming and quiescent galaxies, respectively. The number of star-forming (in blue) and quiescent (in red) galaxies in each mass bin in the combined sample and COSMOS-DASH (C-D) are listed in the upper right of each panel. Note that vdW14/M19 includes both COSMOS-DASH (at $z > 1.5$) and 3D-HST morphologies for the highest-mass bin whereas we consider COSMOS-DASH alone. This therefore explains the lower number of galaxies in our analysis.

measurement acts as a proxy for the completeness of the bin. A higher fraction of galaxies with “usable” morphologies implies the mean size of that bin better conveys the true average size, while the average size of bins with a lower fraction should be treated with caution. Moreover, we only include redshift bins that have 10 or more galaxies in them, so a sufficient sample size is established. The size evolution with redshift is parameterized with a power-law

Table 3

Best-fit Star-forming and Quiescent Size–Evolution Relations for both COSMOS-DASH and the vdW14/M19 Sample, shown in Figure 11

$\log(M/M_\odot)$	Star-forming			
	COSMOS-DASH		vdW14/M19	
	B_z	β_z	B_z	β_z
9.8–10.3	3.96 ± 0.41	0.29 ± 0.14	4.60 ± 0.43	0.54 ± 0.10
10.3–10.8	5.22 ± 0.36	0.47 ± 0.09	4.71 ± 0.35	0.34 ± 0.08
10.8–11.3	7.75 ± 0.40	0.71 ± 0.07	7.90 ± 0.41	0.68 ± 0.06
>11.3	10.66 ± 1.40	0.68 ± 0.13	10.53 ± 1.49	0.64 ± 0.14
$\log(M/M_\odot)$	Quiescent			
	COSMOS-DASH		vdW14/M19	
	B_z	β_z	B_z	β_z
9.8–10.3	1.79 ± 0.03	0.37 ± 0.03	1.74 ± 0.21	0.40 ± 0.19
10.3–10.8	3.12 ± 0.19	0.84 ± 0.09	3.22 ± 0.21	1.08 ± 0.09
10.8–11.3	5.78 ± 0.51	1.06 ± 0.12	6.44 ± 1.02	1.21 ± 0.20
>11.3	10.42 ± 1.78	1.00 ± 0.25	9.53 ± 2.00	0.83 ± 0.24

Note. Relations are given by Equation (10), as described in Section 5.1.

objects with GALFIT flags ≤ 1 (Section 3.1) from the 3D-HST catalogs. The mean size for each mass and redshift bin is then computed and Equation (10) is fit to the running mean size for both quiescent and star-forming galaxies, shown with dashed and dotted black lines in Figure 11, respectively. The number of galaxies used to measure the size-evolution of quiescent and star-forming galaxies for each mass bin and each data set is also indicated in each panel of Figure 11.

In general, the size evolution measured from COSMOS-DASH is remarkably consistent with that from M19, despite that sample being supplemented with deeper data from 3D-HST/CANDELS and COSMOS ACS. This is especially true for star-forming galaxies (see Table 3). We note one regime where the average relations deviate by $\sim 3\sigma$ in β_z : intermediate mass quiescent galaxies (i.e., $10.2 < \log(M_*/M_\odot) < 10.8$). Whereas the vdW14 measurements are based on all five deep CANDELS fields in this stellar mass regime, the COSMOS-DASH data covers a significantly shallower but wider area on-sky for the single COSMOS field. The M19 sample uses COSMOS-DASH data in the most massive bin only, whereas we extend the analysis here to significantly lower stellar masses to test the limits of this data. Within this $10.2 < \log(M_*/M_\odot) < 10.8$ quiescent sample, which shows a slightly higher average size evolution at $0.8 < z < 2$, we also find a higher quiescent fraction. The large, contiguous coverage of the COSMOS-DASH survey, as well as known overdensities within the COSMOS field (e.g., Spitler et al. 2012; Chiang et al. 2014) may account for these larger quiescent fractions found in the COSMOS-DASH sample. Overall, despite some limitations, DASH data is sufficient for recovering these relations down to significantly lower stellar mass limits than previously explored when compared to standard HST observations like 3D-HST.

5.2. The Size-Mass Relation

Another useful test of COSMOS-DASH is examining where in size-mass space DASH morphologies are robust via the fraction of galaxies with low uncertainty ($\delta r_e/r_e < 20\%$). Figure 12 shows the size-mass relation, limiting our sample to nonblended objects (flag_deb=0) with GALFIT flags ≤ 1 .

Using Equation (9), we classify galaxies in the sample as star-forming and quiescent. Sources are separated into three redshift bins and the mean quiescent and star-forming size is measured. Median sizes are only shown in Figure 12 if there are more than 10 objects in the mass bin, and $\geq 80\%$ of the galaxies in the bin have robust size measurements (flag_limit_r=0). Requiring a majority of robust sizes ensures bins with magnitudes fainter than the magnitude limits inferred from Equation (7) on average are excluded and removes an already known sample of sizes potentially dominated by uncertainties.

We investigate the robustness of galaxy structural parameters in 0.5 dex size and stellar mass bins, ranging from ~ 0.3 to 100 kpc and $9 \leq \log(M_*/M_\odot) \leq 12$, respectively. For each region in size-stellar mass parameter space with more than 10 objects, the fraction of galaxies with $(\delta r_e/r_e) < 0.2$ is computed. Regions are then ranked: fractions greater than 0.8 are “usable” and the regions are shaded green in Figure 12, between 0.5 and 0.8 are labeled “problematic” and shaded yellow, and below 0.5 are “unsuitable” and shaded red. Some galaxies with $(\delta r_e/r_e) < 0.2$ may still not have robust morphologies if the effective radius is smaller than the PSF FWHM ($0''.2$). To account for PSF limitations, we also compute the fraction of galaxies in each region with $r_e['] < \text{FWHM}$. This fraction is reflected in the border of the region. Fractions greater than 0.8 have a solid border the same color as the shaded region, while fractions between 0.5 and 0.8 and less than 0.5 have yellow and red dashed borders, respectively.

For low-redshift galaxies, most of the size-mass parameter space explored is usable, with the exception of very large, low-mass galaxies, which are likely nonphysical. These galaxies (as well as intermediate redshift galaxies in a similar parameter space) are likely very faint or noisy, which GALFIT is unable to distinguish from the sky background itself, even after background fitting. The resulting fits attempt to model this, leading to unfeasibly large sizes. For galaxies smaller than 1 kpc, the PSF FWHM becomes an issue as well. This is expected, as lower-redshift ($z < 1$) galaxies, even low-mass galaxies, are usually bright and as such are not limited by the depth of DASH observations. At intermediate redshifts, $1 < z < 2$, the usable parameter space is similar to low redshifts, though the FWHM becomes more of an issue owing to the smaller angular sizes. At high redshifts ($z > 2$), most of the low-mass parameter space becomes problematic, and only galaxies with the highest masses yield robust structural parameters. This is likely due to the fact that higher-redshift galaxies are fainter due to distance, causing the shallower DASH depth to become a limiting factor. In general, large, low-mass galaxies are unreliable due to GALFIT failing to establish a reasonable fit, while the uncertainty in low-mass, high-redshift galaxies is due to shallower imaging as a result of the DASH observation technique. Overall, much of the size-mass parameter space remains usable with DASH, with most issues showing up at $z > 2$.

At all redshifts where galaxies are detectable, DASH imaging complements deeper, smaller area surveys. Due to the shape of the mass function, there are fewer massive galaxies in a given area relative to fainter, lower-mass galaxies. Since a large sample of lower-mass galaxies is obtainable with deeper, narrow-field imaging, standard HST observations are suitable, whereas DASH observations may struggle. Likewise, a large sample of massive galaxies requires a larger area survey,

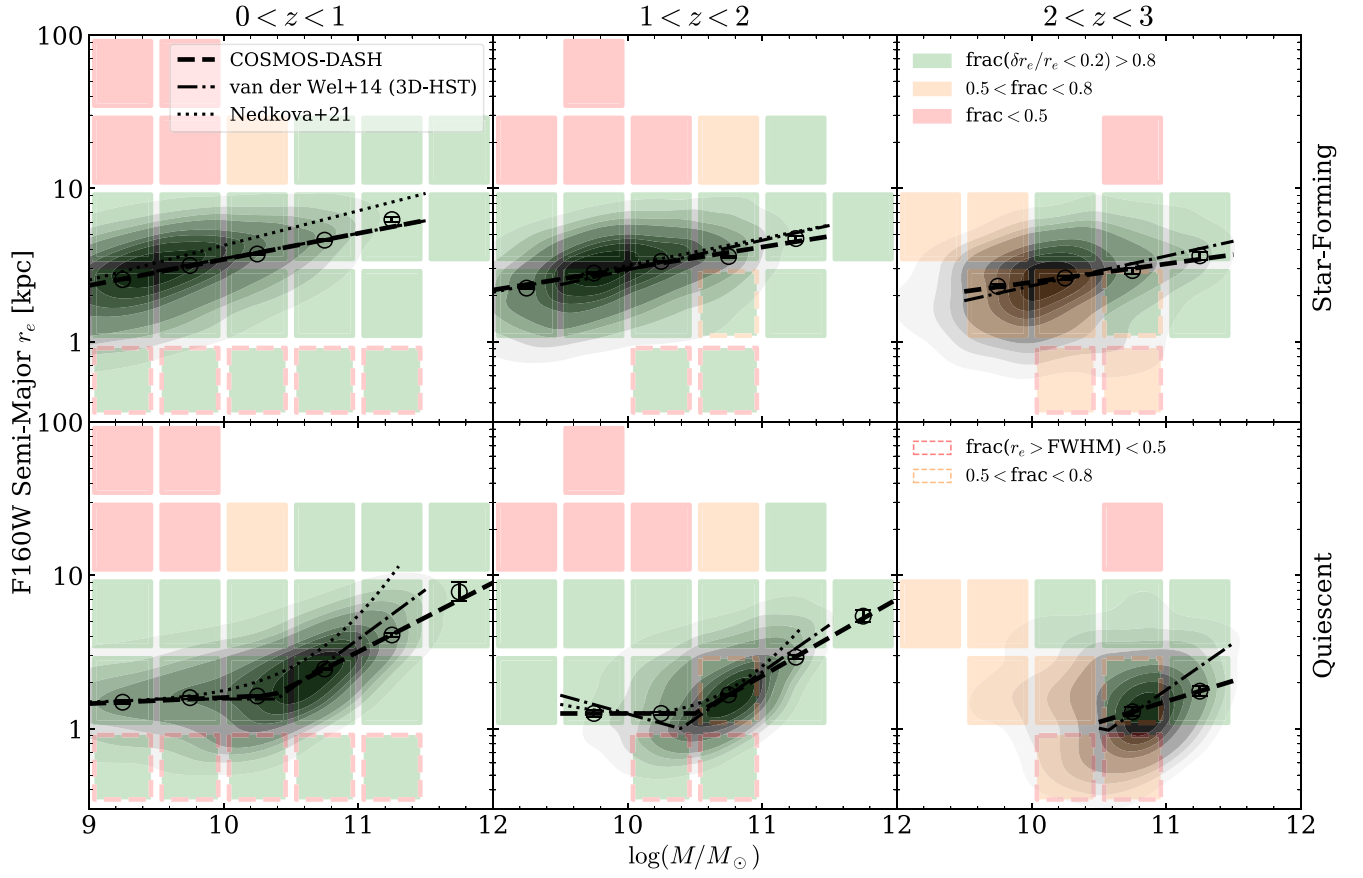


Figure 12. The size-mass relations for star-forming (top row) and quiescent (bottom row) galaxies show COSMOS-DASH sizes are robust for much of the available parameter space. Each column shows galaxies separated into one of three redshift bins: $0 < z < 1$ (left), $1 < z < 2$ (center), and $2 < z < 3$ (right). The underlying distribution of star-forming and quiescent galaxies is shown with contours. Size-mass relations from Nedkova et al. (2021) are included for comparison (dotted lines) alongside refit size-mass relations (to avoid K-corrections) to 3D-HST morphologies (van der Wel et al. 2014). Mass-radius bins are defined by boxes whose colors identify the fraction of galaxies in the bin with fractional size errors less than 20% ($\delta r_e / r_e < 0.2$). Green squares represent a fraction greater than 80%, yellow show a fraction between 50% and 80%, and red indicate a fraction less than 50%, as shown in the legend in the top right of the right panel. Dashed borders around these boxes indicate a significant fraction of galaxies in that bin have an effective radius less than the PSF FWHM ($0''/2$). The color of the dashed border conveys the fraction of galaxies in that bin with $r_e > \text{FWHM}$: red if the fraction is less than 0.5 and yellow if it is between 0.5 and 0.8.

though the depth of standard observations is not required, so DASH observations are better suited. This is utilized in Mowla et al. (2019b), where a combined sample of galaxies with a large mass range is assembled using CANDELS/3D-HST morphologies for lower masses ($\log(M_*/M_\odot) < 11.3$) and COSMOS-DASH morphologies for high-mass galaxies.

Our analysis of the robustness of structural parameter from COSMOS-DASH suggest that the DASH morphological catalog can be used for lower stellar masses than previously explored in the literature. Mowla et al. (2019b) restrict the selection of COSMOS-DASH galaxies to $\log(M_*/M_\odot) > 11.3$ with morphologies from deeper CANDELS/3D-HST catalogs used for lower masses, however our results imply morphologies from COSMOS-DASH, and presumably DASH observations in general, are usable to even $\log(M_*/M_\odot) \sim 9$ for $z < 1$.

We also examine the size-mass relation resulting for both quiescent and star-forming galaxies in each redshift range. For star-forming galaxies we parameterize this equation with a single power law, given by

$$r_e \text{ [kpc]} = A \times m_*^\alpha, \quad (11)$$

where $m_* \equiv M_*/7 \times 10^{10} M_\odot$ (van der Wel et al. 2014; Mowla et al. 2019b). We then fit Equation (11) to the median star-forming sizes and show the best-fit lines with dashed lines

Table 4
Results from Fits to Star-forming and Quiescent Size–Mass Distributions Using Equation (11) and (12)

z	Star-forming			
	A	α		
0–1	4.84 ± 0.08	0.17 ± 0.01		
1–2	4.12 ± 0.15	0.15 ± 0.02		
2–3	3.20 ± 0.09	0.12 ± 0.02		
z	Quiescent			
	A	α_1	α_2	$\log(M_p/M_\odot)$
0–1	1.73 ± 0.04	0.04 ± 0.01	0.45 ± 0.02	10.37 ± 0.03
1–2	1.23 ± 0.03	-0.01 ± 0.02	0.50 ± 0.01	10.50 ± 0.01

(Figure 12). The best-fit parameters for Equation (11) are listed in the top of Table 4. The behavior of COSMOS-DASH quiescent galaxy sizes at $z < 2$ is better described by a broken power law, given by

$$r_e \text{ [kpc]} = \begin{cases} A \times m_*^{\alpha_1} & M_* \leq M_p \\ A \times m_p^{(\alpha_1 - \alpha_2)} \times m_*^{\alpha_2} & M_* > M_p, \end{cases} \quad (12)$$

where m_* is the same as in Equation (11), M_p is the pivot mass in solar masses, and $m_p \equiv M_p/7 \times 10^{10} M_\odot$. We fit this relation to the median quiescent galaxy sizes for the two bins with $z < 2$. Due to a lack of low mass galaxies in the high-redshift bin ($z > 2$), no fit is made. The best-fit relations from Equation (12) are shown with dashed lines in each panel of Figure 12, and the best-fit parameters are given in the bottom of Table 4.

For comparison, we also fit Equation (11) and (12) to the full sample of galaxies from the 3D-HST morphological catalogs (van der Wel et al. 2014), again using uncorrected sizes. These relations, as well as the size-mass relations from Nedkova et al. (2021), are shown with dotted and dashed-dotted lines in Figure 12, respectively. In general, there is good agreement between star-forming size-mass relations at all redshifts. Quiescent size-mass relations are also in agreement at low masses, but the high-mass end shows noticeable deviations. This is discussed in Mowla et al. (2019b), who compare size-mass relations using high-mass COSMOS-DASH galaxies to those from van der Wel et al. (2014). The larger sample of high-mass galaxies obtained with DASH observations may provide a more accurate measurement of the size-mass relation in this mass range and thus explain the discrepancy. However, it may also to some degree be due to contamination when identifying star-forming and quiescent galaxy populations (as noted in Mowla et al. 2019b).

The result of this broken power-law relation is a flattening of the size-mass relation for quiescent galaxies below $\sim 3 \times 10^{10} M_\odot$. This behavior has been noted previously in the literature (e.g., Dutton et al. 2011; Cappellari et al. 2013; Norris et al. 2014; Whitaker et al. 2017; Nedkova et al. 2021). Broken power-law relations for all galaxies are also found in Mowla et al. (2019a), with the pivot proposed to mark the transition from star formation to the dry merger dominated mode of growth for galaxies. This earlier study also compares the size-mass relation to the stellar mass-halo mass relation and finds comparable slopes and pivots between the two relations. Further theoretical support of the flattening of the low-mass quiescent size-mass relation is found in results of simulations (Shankar et al. 2014; Furlong et al. 2017; Genel et al. 2018). This flattening is likely to be physical and not a result of inaccurate size measurements for small, low-mass galaxies (e.g., van der Wel et al. 2014; Whitaker et al. 2017). We perform a comparative analysis of quiescent galaxy sizes (observed F160W frame) relative to the 3D-HST morphological catalog (van der Wel et al. 2014), which yields a similar flattened size-mass relation at low stellar masses.

A potential cause of this phenomenon could be the environment in which these low-mass galaxies are embedded. There are many ways to form and quench galaxies, and likely different physical processes for cluster and field galaxies (e.g., Peng et al. 2010b; Tal et al. 2014; van Dokkum et al. 2015; Bluck et al. 2020; McNab et al. 2021). Thus, the morphologies of galaxies in different environments could vary. Moreover, as galaxies evolve, their morphologies may change as well (Dressler 1980; Postman et al. 2005). For example, dry mergers can significantly increase the size of quiescent galaxies (Bezanson et al. 2009; Cappellari 2013), while gas-rich mergers or violent disk instabilities are proposed physical drivers reducing the effective radius of compact star-forming galaxies (Barro et al. 2013). We explore the role of environment on quiescent galaxy size in the next section.

5.3. Environmental Effects

To investigate the environmental dependence of the flattening of the quiescent size-mass relation, COSMOS-DASH galaxies with $z < 1.2$ and GALFIT flags ≤ 1 are matched within a $0''.5$ radius to the publicly available COSMOS density field catalog (Darvish et al. 2015, 2017). Since redshift precision is important in determining the galactic density field, we cross match first spatially (using R.A. and decl.) and then with photometric redshift, discarding galaxies that exhibit a redshift difference of $\Delta z > 0.1$ between the two catalogs. This second check removes $\sim 5\%$ of galaxies that are cross-matched by R.A. and decl. alone. We then examine the correlation between a number of structural and environmental parameters available for this sample of quiescent galaxies. The parameters used are the size, Sérsic index, axis ratio, $U - V$ and $V - J$ color, and the overdensity ($\delta = \Sigma/\Sigma_{\text{median}}$). These correlations are examined for three mass bins: low mass ($\log(M/M_\odot) < 10$), intermediate mass ($10 < \log(M/M_\odot) < 11$), and high mass ($\log(M/M_\odot) > 11$), indicated with solid black histograms, dashed black histograms/contours, and orange histograms, respectively, in Figure 13.

Figure 13 highlights different structural parameter distributions (size, Sérsic index, and axis ratio) for low- and high-mass quiescent galaxies. Lower mass galaxies preferentially have smaller sizes overall, as expected, though these sizes are also similar to intermediate-mass galaxies. This reinforces a flattening of the size-mass relation at low masses. We also find low-mass quiescent galaxies have morphologies similar to star-forming galaxies (smaller Sérsic index and axis ratio), while their high-mass counterparts are more elliptical in nature (larger Sérsic index and axis ratio). In general, the distribution of overdensity should be centered around $\delta = 1$, since overdensity is defined relative to the median density at a given redshift. However, the distribution of overdensities for low- and high-mass galaxies are skewed, with low-mass quiescent galaxies being more abundant in field ($\delta \lesssim 1$) environments and high-mass galaxies being more abundant in cluster ($\delta \gtrsim 3$) environments.

One explanation for the deficit of low-mass quiescent galaxies in the highest overdensities could be the preferential destruction of satellite galaxies in clusters via tidal interactions and/or mergers with other cluster galaxies. Matharu et al. (2019) found that a significant fraction of compact quiescent cluster galaxies must be destroyed in order to maintain the observed consistency between field and cluster size-mass relations (see also, e.g., Weinmann et al. 2009; Maltby et al. 2010; Cebrián & Trujillo 2014). We separate our sample of quiescent galaxies into quartiles of increasing axis ratio (top) and Sérsic index (bottom) and show the resulting size-mass relations in Figure 14.

A flattening in the size-mass relation of quiescent galaxies is observed for all Sérsic index bins except for the most centrally concentrated galaxies. The size-mass relation for quiescent galaxies with $4 < n < 6$ results because the lowest-mass galaxies are slightly more compact, while galaxies close to the pivot mass are slightly larger on average, thereby returning the relation to a power law. Interestingly, the flattening is still present in the 50% galaxies with high axis ratios ($q > 0.62$). This is driven by face-on disk galaxies, which dominate the low-mass quiescent population: when removing galaxies with $n < 2.5$ from the axis ratio analysis, the flattening disappears for $q > 0.62$. Quiescent galaxies with lower Sérsic indices ($n < 2.5$) have been measured with a wide range axis ratios, as

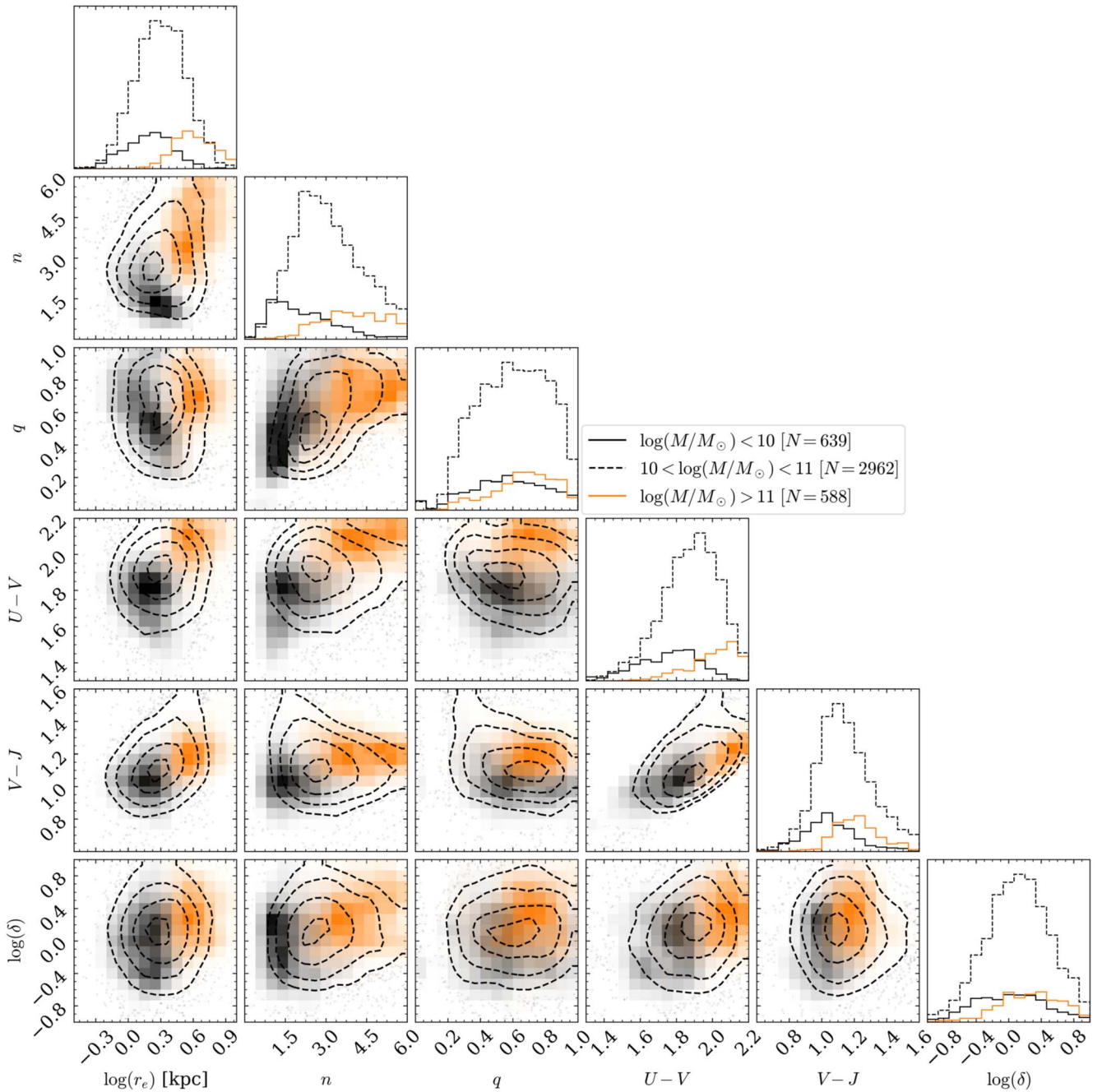


Figure 13. Quiescent galaxies of different mass have different structural properties, as shown in the covariances of various parameters. The included structural and environmental parameters are effective radius, Sérsic index, axis ratio, $U-V$ and $V-J$ color, and galaxy field overdensity ($\delta = \Sigma/\Sigma_{\text{median}}$). Low-mass ($\log(M_*/M_\odot) < 10$) and high-mass ($\log(M_*/M_\odot) > 11$) galaxies are shown with black and orange 1D and 2D histograms, respectively. Dashed contours and 1D histograms indicate intermediate-mass galaxies ($10 < \log(M_*/M_\odot) < 11$). The number of galaxies in each mass bin is shown in the legend.

well as a roughly even distribution over this range (see Figure 3 in Chang et al. 2013). Thus, it is feasible that this sample contains a significant amount of high-axis-ratio, low-Sérsic-index galaxies. These face-on disk galaxies will have comparable axis ratios to centrally concentrated galaxies ($n > 2.5$), but are noticeably larger in size. Likewise, when galaxies with $n > 2.5$ are removed, the flattening becomes significantly stronger. With the mean overdensity of the galaxies shown within hexagonal bins, we also find that these higher-Sérsic-index galaxies inhabit denser environments on average. We note that separating the sample into finer redshift bins does not change the general results of this analysis.

The over-representation of high-Sérsic-index galaxies in the densest environments (Figure 13), as well as the existence of compact, centrally concentrated quiescent galaxies in clusters (e.g., right panel in Figure 14; see also Matharu et al. 2019), may result if disk quiescent galaxies are either preferentially destroyed via mergers or prevented from maintaining a stable disk due to tidal interactions.

Since cluster galaxies do not exhibit a significant increase in size due to minor mergers (Matharu et al. 2019), compact cluster galaxies that are not destroyed would retain their smaller sizes. Together, this could explain the disappearance of the flattening at the highest Sérsic indices; compact elliptical

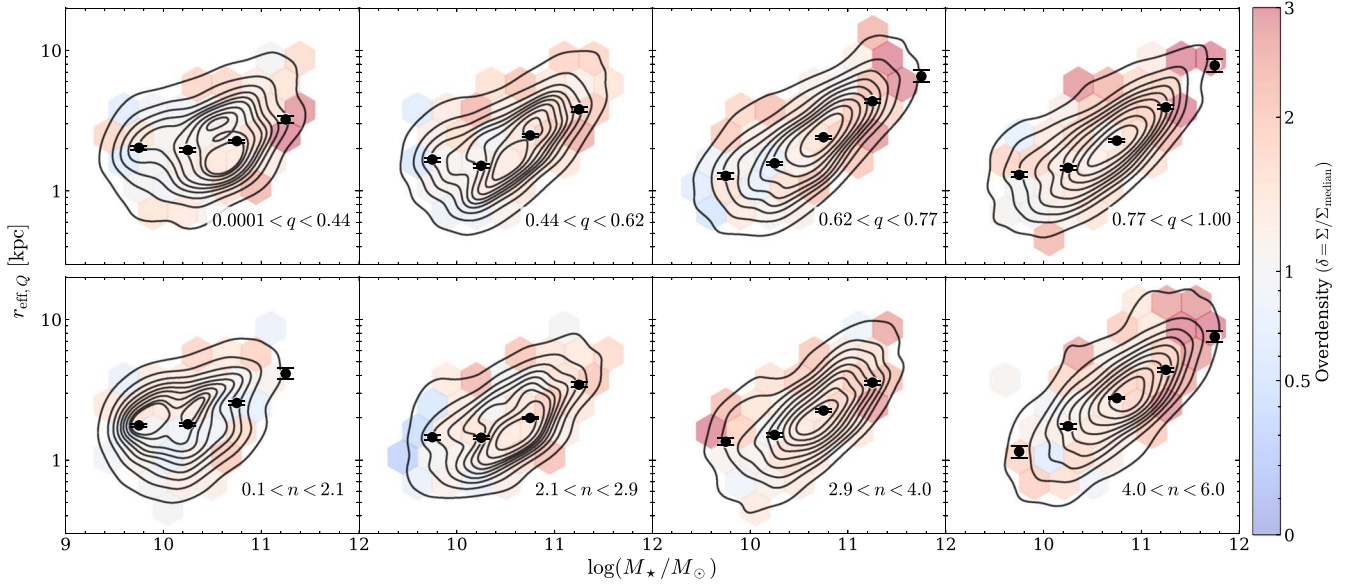


Figure 14. The flattening of the size-mass relation for quiescent galaxies at $z < 1.2$ may disappear in galaxies with high Sérsic indices. Galaxies are separated by axis ratio (top) and Sérsic index (bottom) into approximately equal number quartiles indicated in each panel. Empty KDE contours show the underlying distribution of sizes. For each quartile, running medians are shown with solid points, and error bars show the 1σ SEM. Hexagonal bins indicate the average overdensity ($\delta = \Sigma/\Sigma_{\text{median}}$) of points within the bin, as indicated by the color bar.

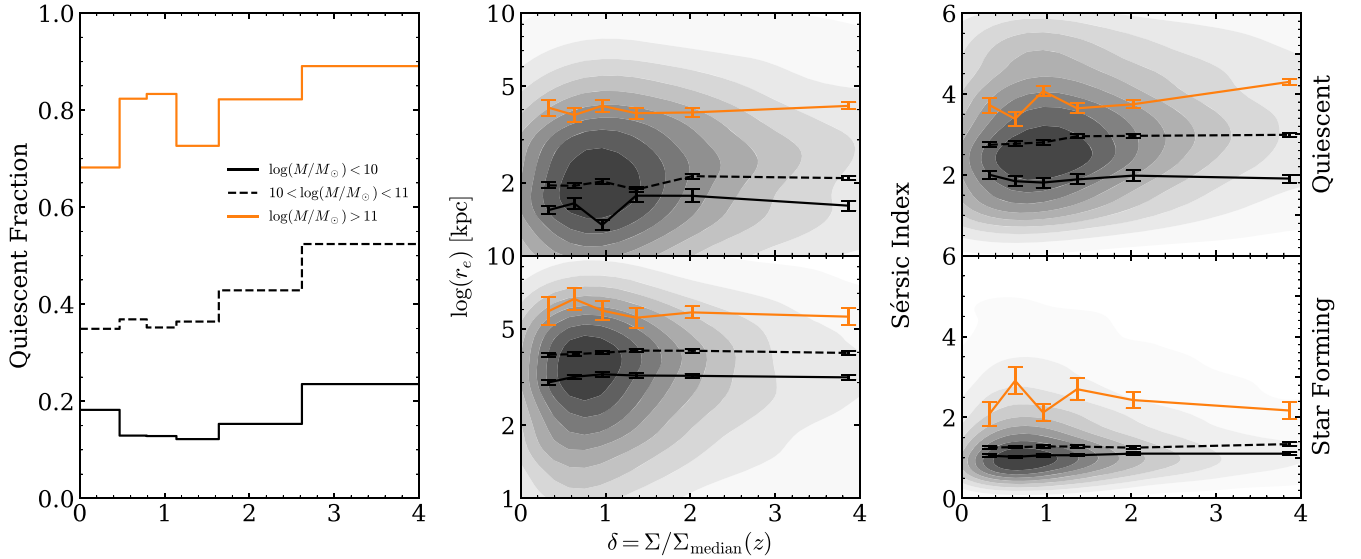


Figure 15. The constant evolution of low- ($\log(M/M_\odot) < 10$), intermediate- ($10 < \log(M/M_\odot) < 11$), and high- ($\log(M/M_\odot) > 11$) mass galaxy properties with density suggests environmental effects are not a dominant mechanism behind the flattening of the quiescent size-mass relation. The three mass regimes are represented with solid black, dashed black, and solid orange lines, respectively. The left panel shows the change in quiescent fraction for each mass bin. The other panels show the change in size (middle column) and Sérsic index (right column) for both quiescent (top row) and star-forming galaxies (bottom row). The total distributions of quiescent and star-forming sizes and Sérsic indices are shown with shaded contours.

quiescent galaxies are less likely to be destroyed in clusters, and the dynamics of the cluster effectively “freeze” their sizes, leading to a single power-law quiescent size-mass relation.

However, the preferential destruction of diskier quiescent galaxies in dense environments should also manifest with increasing Sérsic index with density. Likewise, if the larger low-Sérsic-index galaxies are destroyed in the dense environments, we would expect that low-mass sizes decrease with increasing density. We see no evidence for such a trend in Figure 15, which shows the dependence of quiescent fraction (left), size (middle) and Sérsic index (right) on overdensity. For the lowest-mass bin (black solid line), the quiescent fraction

remains relatively constant with overdensity, suggesting that the environment does not play a significant role in the quenching of the least massive galaxies. Moreover, both the size and Sérsic index of similar mass quiescent (top) and star-forming galaxies (bottom) is constant with density for all mass bins. These results imply environment is not the dominant effect producing the flattening of the quiescent size-mass relation at low masses. Though environmental effects may still be significant for some galaxies, universally other processes must drive this behavior. This agrees with the results of Huertas-Company et al. (2013), who find that the size-mass relation of massive ($\log(M_*/M_\odot) > 10.5$) early-type galaxies

has no significant dependence on environment at $z < 0.09$ (see also, Maltby et al. 2010; Fernández Lorenzo et al. 2013; Shankar et al. 2014).

If environment is not driving the flattening, it may instead be related to in situ physical processes. Studies have shown that the flattening of the size-mass relation is correlated with growth due to star formation, whereas high mass growth is thought to be merger driven (e.g., van Dokkum et al. 2015; Mowla et al. 2019a). This sets up a narrative where internal processes dominate at lower-mass scales whereas extrinsic factors dominate the evolution of the most massive galaxies. The resulting size-mass relation for quiescent galaxies could thus be explained by quenching of low-mass galaxies via the depletion of gas reservoirs, with no replenishment. Another alternative is that this gas is instead stabilized due to the formation of a bulge and thereby inefficient at forming new generations of stars (e.g., Martig et al. 2009), under the assumption that a Sérsic index of 2 corresponds to a bulge that is sufficiently large. In both instances, the quenching process occurs without mergers, so galaxies remain in a similar location in size-mass parameter space and the shallower slope of the star-forming size-mass relation is retained. While we cannot discern the physical process responsible for this flattening in the quiescent sample within the data set at hand, we can rule out environment as the primary driving factor.

6. Summary

We present a public release of the morphological catalog for the COSMOS-DASH survey obtained with 2D-Sérsic fits using GALFIT (Peng et al. 2002, 2010a) for 51,586 galaxies. Using a combination of bootstrapping with GALFIT and comparing morphologies of galaxy analog populations, we obtain parameter errors consistent with those from the CANDELS/3D-HST morphological catalog (van der Wel et al. 2012, 2014). We analyze the various limits and parameter space for which these structural measurements and their errors are robust. The wider area, albeit shallower, imaging attainable with DASH is useful for observing a significant sample of high-mass, bright galaxies, which are less common in a given area of the sky. This allows DASH observations to work in tandem with standard HST observations: the deeper, standard imaging can obtain significant samples of low-mass, faint sources, while wider-area DASH observations obtain a sample of high-mass galaxies.

However, DASH observations are also capable of producing results for a wide range of galaxy masses and sizes, as shown in Figure 12. Analysis of the limits of COSMOS-DASH morphologies suggests sizes and Sérsic indices are usable to a limiting magnitude of roughly 23 and 22 ABmag for the shallowest DASH observations, respectively. We find DASH sizes at $z < 2$ are usable for $\log(M_*/M_\odot) > 9$ and at higher redshifts for $\log(M_*/M_\odot) > 10.5$. Our analysis also indicates that large, unphysical sizes are mainly due to issues with GALFIT, while unusable sizes at higher redshifts are primarily driven by the shallower depth of the COSMOS-DASH survey due to the DASH technique. Overall, the shallower depth and complex data reduction of DASH observations does not prevent high-fidelity measurements of galaxy morphology using DASH data.

With the COSMOS-DASH morphological catalog, we observe a flattening of the size-mass relation for quiescent galaxies at low masses ($\log(M_*/M_\odot) < 10.5$), similar to

existing results from observations (e.g., Cappellari et al. 2013; Norris et al. 2014; Lange et al. 2015; Whitaker et al. 2017; Nedkova et al. 2021) and simulations (e.g., Shankar et al. 2014; Furlong et al. 2017). Combining COSMOS-DASH morphologies with galaxy density field measurements (Darvish et al. 2015, 2017), we investigate the dependence of this low-mass flattening on environment. Correlations between structural and environmental parameters suggest distinct morphological populations for low- and high-mass quiescent galaxies, with low-mass galaxies having significantly smaller Sérsic indices and axis ratios. Moreover, these correlations also indicate that these low-mass quiescent galaxies are more prevalent in underdense environments, relative to their high-mass counterparts.

Analyzing the evolution of the quiescent size-mass relation with Sérsic index and environment, we find a disappearance of the low-mass flattening for the highest-Sérsic-index galaxies. These centrally concentrated objects are also more likely to inhabit denser environments than their lower-Sérsic-index counterparts. Results from other studies (e.g., Weinmann et al. 2009; Maltby et al. 2010; Cebrián & Trujillo 2014; van der Wel et al. 2014; Matharu et al. 2019) imply the majority of satellite galaxies in clusters (dense environments) must be destroyed by $z \sim 0$ to match observed size-mass relations. Preferential destruction of compact low-Sérsic-index galaxies through tidal interactions or mergers would lead to both an over-representation of compact centrally concentrated galaxies in clusters, as well as a disappearance in the size-mass flattening for high-Sérsic-index galaxies. However, the average quiescent fractions, sizes, and Sérsic indices for both quiescent and star-forming galaxies are all roughly constant with overdensity. Taken together, this suggests that the main driver of the flattening of the quiescent size-mass relation at low stellar masses is not environment (see also Fernández Lorenzo et al. 2013). Instead, internal physical processes are likely the cause of the flattening, though exactly which processes are responsible is outside the scope of this work.

This paper is based on observations made with the NASA/ESA HST, obtained at the Space Telescope Science Institute, which is operated by the Association of Universities for Research in Astronomy, Inc., under NASA contract NAS 5-26555. These observations are associated with program HST-GO-14114. Support for GO-14114 is gratefully acknowledged. S.C. and K.W. wish to acknowledge funding from the Alfred P. Sloan Foundation grant Nos. FG-2019-12514, HST-AR-15027, and HST-GO-16259. MA acknowledges support by NASA under award No 80NSSC19K1418. M.S. and K.W. acknowledge support under NASA grant No. 80NSSC20K0416. This research made use of Montage. It is funded by the National Science Foundation under grant No. ACI-1440620 and was previously funded by the National Aeronautics and Space Administrations Earth Science Technology Office, Computation Technologies Project, under Cooperative Agreement No. NCC5-626 between NASA and the California Institute of Technology. The Cosmic Dawn Center is funded by the Danish National Research Foundation under grant No. 140.

Appendix Background Pedestal

Previous studies have shown it is important to let GALFIT fit a constant sky background as a free parameter (Häussler et al. 2007). In order to understand the effects of allowing GALFIT

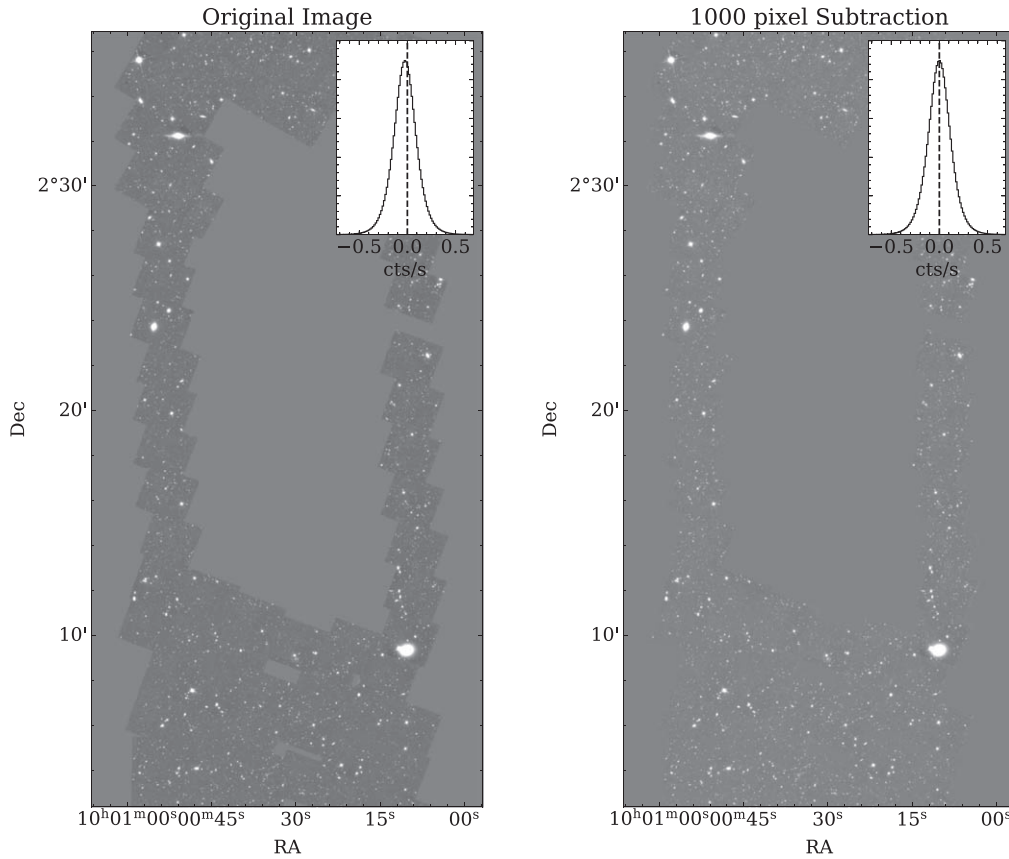


Figure A1. Comparison of the DASH-only reduction of the calibration field before (left) and after (right) background subtraction. The images have the same scale limits, which highlights the slightly negative background in the left panel. The inset histograms show the distribution of background pixels (i.e., any pixel with a value of 0 in the segmentation map). A slight background of $-0.0252 \text{ cts s}^{-1}$ is apparent in the histogram in the left panel. This background is much smaller than the standard deviation in background pixels ($0.1465 \text{ cts s}^{-1}$) and is successfully subtracted in the right inset histogram.

to fit the background in more detail we conduct a series of tests. First, estimates of the mean background in the total COSMOS-DASH mosaic are made. Sources are excluded using a combination of the segmentation map and sigma clipping. Bad pixels and empty regions are excluded by removing pixels where the weight map is zero. Separate estimates are made for the DASH and CANDELS regions of the mosaic using a second weight map selection. Low-weight pixels are attributed to DASH-obtained data and high-weight pixels to CANDELS. The estimated mean DASH background is -0.0252 ± 0.1465 , while CANDELS is 0.0011 ± 0.0694 , indicating this DASH data has a more significant background than CANDELS and more variation in the background. This is likely due to the shallower depth of DASH observation caused by shorter exposure times. The DASH background also does not vary significantly as a function of the location in the image.

We perform a standard background subtraction on both the DASH- and CANDELS-only calibration field reductions. Background meshes with bin sizes of 200, 400, 600, 800, 1000, and 1200 pixels are applied to both reductions and the distribution of background fluxes are computed. The 1000 bin mesh is chosen, as the background-subtracted image for this mesh has a mean background closest to zero. A comparison of the DASH-only reduction before (left) and after (right) background subtraction is shown in Figure A1. First, the GALFIT pipeline is run on the 483 galaxies in the background-subtracted calibration field with the GALFIT sky background fixed to zero. Comparing the resulting best-fit effective radii

and Sérsic indices to the CANDELS/3D-HST morphological catalog (van der Wel et al. 2012) and high-mass galaxies from COSMOS-DASH (Mowla et al. 2019b), shows that both the radius and Sérsic indices are roughly 0.1 and 0.2 dex smaller in DASH, respectively. We then run GALFIT with sky background as a free parameter on the background-subtracted calibration field, finding good agreement with CANDELS/3D-HST. The mean GALFIT-determined sky background is -0.0206 ± 0.0108 , despite measuring a negligible background when the 1000 bin mesh background is subtracted (see also Figure 4, bottom). Similar negligible backgrounds are also measured with the other subtractions. This suggests that this small background value is leading to the significant difference in our measured morphologies.

To further characterize the background of the DASH-only reduction, we use the empty apertures approach from Section 3.3 on the background subtracted image. This is done in the DASH-only reduction of the calibration field, which allows for direct comparison with CANDELS (see Figure A2). Of interest to this section is the change in the average background, as indicated with the shift in the peak of the distribution toward slightly negative values at larger aperture sizes. An increased average background for larger apertures could indicate that measuring the background with a smaller aperture size underestimates the actual background level. However, Figure 4 (bottom) shows that the average background per pixel is roughly (but not quite) constant with aperture size, and is approximately zero. This behavior is also

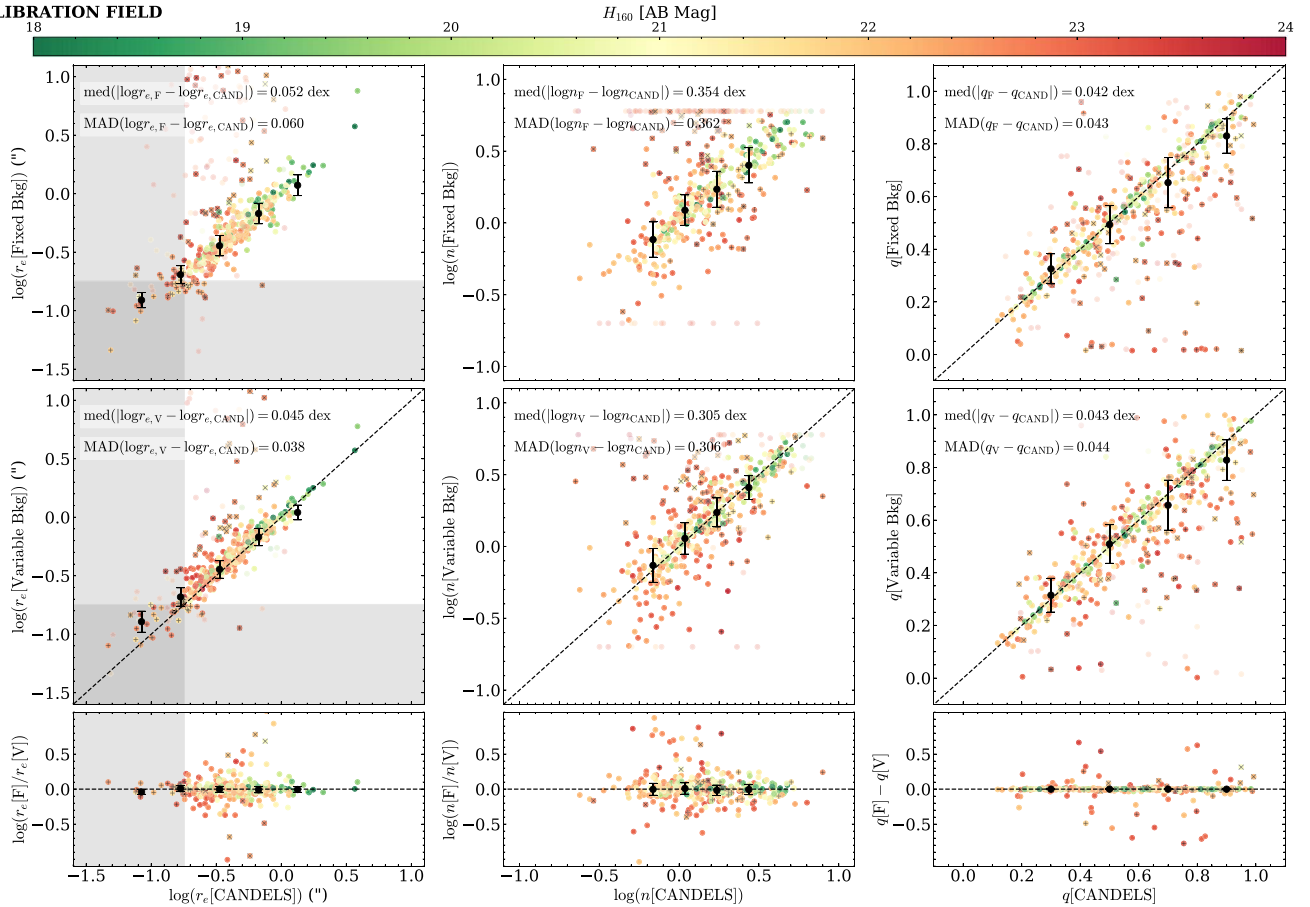


Figure A2. Comparison of the best fit GALFIT parameters of the 483 calibration galaxies in the DASH-only reduction using two different methods to deal with the background; the small scatter in the middle row implies that the background should be treated as a free parameter in GALFIT. The top and middle rows show the effective radii, Sérsic indices, and axis ratios of the best fit Sérsic models determined with (top) and without (middle) fixed backgrounds, respectively, compared to those from CANDELS/3DHST (van der Wel et al. 2014). Transparent points are those with `flag=2` parameter values (see Section 3.1). The bottom row shows the difference in the parameters when measured both with and without fitting background. The large black points are the running median in each bin, with errorbars showing the scatter determined by the MAD of the bin. The color scale indicates the H_{160} magnitude of the source in AB magnitudes. Points with black x's are those that are greater than 0.3 dex from the one-to-one line in radius. The gray shaded region shows radii less than the PSF FWHM and points with black +s are sources whose best fit radius falls in this region. Text in the top and middle row indicates the median and scatter in the offset between CANDELS/3D-HST parameters and parameters derived using the two methods to deal with the background.

independent of the overall bin size used to perform the background subtraction. A comparison with the GALFIT background pedestal is also shown, consistent within 2σ . A potential cause of the discrepancy between the GALFIT and empty aperture backgrounds could be that the empty apertures are not empty and contain faint wings from galaxies (potentially due to inadequate masking).

Next, we investigate whether or not this GALFIT background is something that GALFIT consistently measures from the data, or if GALFIT will only produce reasonable fits if it is allowed to fit a constant sky background. To check this, we run GALFIT twice on calibration field galaxies using the background subtracted DASH-only reduction. In the first run, we allow GALFIT to fit the background. In the second run, we remove the GALFIT-measured constant sky background (see bottom panel of Figure 4) from the data and fix the background parameter to zero. In Figure A2, the radius, Sérsic index, and axis ratio of these two fitting methods are compared to each other and the CANDELS/3D-HST Sérsic parameters (van der Wel et al. 2012, 2014). The top and middle rows of Figure A2 compare the parameters from the run with a fixed and variable (fit by GALFIT) background to the CANDELS/3D-HST morphological parameters, in a similar layout to Figure 6.

The bottom row compares the difference between the parameters both with and without fixing the background relative to measurements from CANDELS/3D-HST. All panels indicate no systematic offset, both between the different methods to deal with background and between CANDELS/3D-HST and our morphologies.

In general, both methods show consistency with the measured CANDELS/3D-HST morphologies, suggesting that the small background value measured by GALFIT (see bottom panel of Figure 4) is the root cause of the offset we observed prior. The largest scatter is in Sérsic index, as this parameter is the most sensitive to the measure of the background. With an incorrect background estimate, the combination of a low Sérsic index and faint background flux can appear similar to a large Sérsic index with faint wings. The scatter in the parameters is smaller for radius when we allow GALFIT to fit a background: the fixed background approach has a 9% larger scatter in radius and a 20% larger scatter in Sérsic index. Moreover, 12% of galaxies with the fixed background are more than 0.3 dex from CANDELS/3D-HST, while only 8% with a variable background deviate by this much. The median offset from CANDELS/3D-HST (Figure A2, text in top and middle rows) also prefers a variable background. This suggests it is

preferable to allow GALFIT to deal with the background. Similarly, Häussler et al. (2007) conclude that GALFIT performs significantly better when allowed to internally measure a sky background, as opposed to being provided a fixed background (e.g., from SExtractor in their case). Given the smaller spread in morphological parameters and the findings of Häussler et al. (2007), we therefore adopt the background fitting in GALFIT to ensure consistent fits that are not biased by the choice of constant background pedestal. Moreover, this analysis also shows that GALFIT consistently recovers morphological parameters when fitting a background regardless of the initial background subtraction. As such, we do not use a background subtracted version of the full COSMOS-DASH mosaic when determining morphologies for the full sample, since GALFIT needs to fit a background regardless of prior subtraction, and the background pedestal in the calibration field is roughly constant.

ORCID iDs

Sam E. Cutler  <https://orcid.org/0000-0002-7031-2865>
 Katherine E. Whitaker  <https://orcid.org/0000-0001-7160-3632>
 Lamiya A. Mowla  <https://orcid.org/0000-0002-8530-9765>
 Gabriel B. Brammer  <https://orcid.org/0000-0003-2680-005X>
 Arjen van der Wel  <https://orcid.org/0000-0002-5027-0135>
 Danilo Marchesini  <https://orcid.org/0000-0001-9002-3502>
 Pieter G. van Dokkum  <https://orcid.org/0000-0002-8282-9888>
 Ivelina G. Momcheva  <https://orcid.org/0000-0003-1665-2073>
 Mimi Song  <https://orcid.org/0000-0002-8442-3128>
 Mohammad Akhshik  <https://orcid.org/0000-0002-3240-7660>
 Erica J. Nelson  <https://orcid.org/0000-0002-7524-374X>
 Rachel Bezanson  <https://orcid.org/0000-0001-5063-8254>
 Marijn Franx  <https://orcid.org/0000-0002-8871-3026>
 Mariska Kriek  <https://orcid.org/0000-0002-7613-9872>
 Joel Leja  <https://orcid.org/0000-0001-6755-1315>
 John W. MacKenty  <https://orcid.org/0000-0001-6529-8416>
 Adam Muzzin  <https://orcid.org/0000-0002-9330-9108>

References

- Anderson, J. 2016, Empirical Models for the WFC3/IR PSF, Space Telescope WFC Instrument Science Report
- Barro, G., Faber, S. M., Koo, D. C., et al. 2017, *ApJ*, **840**, 47
- Barro, G., Faber, S. M., Pérez-González, P. G., et al. 2013, *ApJ*, **765**, 104
- Bell, E. F., van der Wel, A., Papovich, C., et al. 2012, *ApJ*, **753**, 167
- Bertin, E., & Arnouts, S. 1996, *A&AS*, **117**, 393
- Bezanson, R., van Dokkum, P. G., Tal, T., et al. 2009, *ApJ*, **697**, 1290
- Bluck, A. F. L., Maiolino, R., Piotrowska, J. M., et al. 2020, *MNRAS*, **499**, 230
- Brammer, G. B., van Dokkum, P. G., Franx, M., et al. 2012, *ApJS*, **200**, 13
- Cappellari, M. 2013, *ApJL*, **778**, L2
- Cappellari, M., McDermid, R. M., Alatalo, K., et al. 2013, *MNRAS*, **432**, 1862
- Cassata, P., Giavalisco, M., Guo, Y., et al. 2011, *ApJ*, **743**, 96
- Cebrián, M., & Trujillo, I. 2014, *MNRAS*, **444**, 682
- Chabrier, G. 2003, *PASP*, **115**, 763
- Chang, Y.-Y., van der Wel, A., Rix, H.-W., et al. 2013, *ApJ*, **773**, 149
- Chen, Z., Faber, S. M., Koo, D. C., et al. 2020, *ApJ*, **897**, 102
- Chiang, Y.-K., Overzier, R., & Gebhardt, K. 2014, *ApJL*, **782**, L3
- Darvish, B., Mobasher, B., Martin, D. C., et al. 2017, *ApJ*, **837**, 16
- Darvish, B., Mobasher, B., Sobral, D., Scoville, N., & Aragon-Calvo, M. 2015, *ApJ*, **805**, 121
- Dimauro, P., Huertas-Company, M., Daddi, E., et al. 2018, *MNRAS*, **478**, 5410
- Dimauro, P., Huertas-Company, M., Daddi, E., et al. 2019, *MNRAS*, **489**, 4135
- Dressler, A. 1980, *ApJ*, **236**, 351
- Dutton, A. A., van den Bosch, F. C., Faber, S. M., et al. 2011, *MNRAS*, **410**, 1660
- Fernández Lorenzo, M., Sulentic, J., Verdes-Montenegro, L., & Argudo-Fernández, M. 2013, *MNRAS*, **434**, 325
- Furlong, M., Bower, R. G., Crain, R. A., et al. 2017, *MNRAS*, **465**, 722
- Genel, S., Nelson, D., Pillepich, A., et al. 2018, *MNRAS*, **474**, 3976
- Häussler, B., McIntosh, D. H., Barden, M., et al. 2007, *ApJS*, **172**, 615
- Hill, A. R., Muzzin, A., Franx, M., et al. 2017, *ApJ*, **837**, 147
- Holwerda, B. W., Bouwens, R., Oesch, P., et al. 2015, *ApJ*, **808**, 6
- Huertas-Company, M., Shankar, F., Mei, S., et al. 2013, *ApJ*, **779**, 29
- Kartaltepe, J. S., Dickinson, M., Alexander, D. M., et al. 2012, *ApJ*, **757**, 23
- Koekemoer, A. M., Aussel, H., Calzetti, D., et al. 2007, *ApJS*, **172**, 196
- Koekemoer, A. M., Faber, S. M., Ferguson, H. C., et al. 2011, *ApJS*, **197**, 36
- Kriek, M., van Dokkum, P. G., Labbé, I., et al. 2009, *ApJ*, **700**, 221
- Lange, R., Driver, S. P., Robotham, A. S. G., et al. 2015, *MNRAS*, **447**, 2603
- Maltby, D. T., Aragón-Salamanca, A., Gray, M. E., et al. 2010, *MNRAS*, **402**, 282
- Marsan, Z. C., Marchesini, D., Muzzin, A., et al. 2019, *ApJ*, **871**, 201
- Martig, M., Bournaud, F., Teyssier, R., & Dekel, A. 2009, *ApJ*, **707**, 250
- Matharu, J., Muzzin, A., Brammer, G. B., et al. 2019, *MNRAS*, **484**, 595
- McCracken, H. J., Milvang-Jensen, B., Dunlop, J., et al. 2012, *A&A*, **544**, A156
- McNab, K., Balogh, M. L., van der Burg, R. F. J., et al. 2021, *MNRAS*, **508**, 157
- Momcheva, I. G., Brammer, G. B., van Dokkum, P. G., et al. 2016, *ApJS*, **225**, 27
- Momcheva, I. G., van Dokkum, P. G., van der Wel, A., et al. 2017, *PASP*, **129**, 015004
- Mowla, L., van der Wel, A., van Dokkum, P., & Miller, T. B. 2019a, *ApJL*, **872**, L13
- Mowla, L. A., van Dokkum, P., Brammer, G. B., et al. 2019b, *ApJ*, **880**, 57
- Muzzin, A., Marchesini, D., Stefanon, M., et al. 2013a, *ApJ*, **777**, 18
- Muzzin, A., Marchesini, D., Stefanon, M., et al. 2013b, *ApJS*, **206**, 8
- Nedkova, K. V., Häußler, B., Marchesini, D., et al. 2021, *MNRAS*, **506**, 928
- Nelson, E. J., van Dokkum, P. G., Förster Schreiber, N. M., et al. 2016, *ApJ*, **828**, 27
- Norris, M. A., Kannappan, S. J., Forbes, D. A., et al. 2014, *MNRAS*, **443**, 1151
- Peng, C. Y., Ho, L. C., Impey, C. D., & Rix, H.-W. 2002, *AJ*, **124**, 266
- Peng, C. Y., Ho, L. C., Impey, C. D., & Rix, H.-W. 2010a, *AJ*, **139**, 2097
- Peng, Y.-j., Lilly, S. J., Kovač, K., et al. 2010b, *ApJ*, **721**, 193
- Postman, M., Franx, M., Cross, N. J. G., et al. 2005, *ApJ*, **623**, 721
- Scoville, N., Aussel, H., Brusa, M., et al. 2007, *ApJS*, **172**, 1
- Shankar, F., Mei, S., Huertas-Company, M., et al. 2014, *MNRAS*, **439**, 3189
- Shibuya, T., Ouchi, M., & Harikane, Y. 2015, *ApJS*, **219**, 15
- Shingley, H. V., Lange-Vagle, D., Marchesini, D., et al. 2018, *ApJS*, **235**, 14
- Skelton, R. E., Whitaker, K. E., Momcheva, I. G., et al. 2014, *ApJS*, **214**, 24
- Spitler, L. R., Labbé, I., Glazebrook, K., et al. 2012, *ApJL*, **748**, L21
- Suess, K. A., Kriek, M., Price, S. H., & Barro, G. 2019a, *ApJ*, **877**, 103
- Suess, K. A., Kriek, M., Price, S. H., & Barro, G. 2019b, *ApJL*, **885**, L22
- Tal, T., Dekel, A., Oesch, P., et al. 2014, *ApJ*, **789**, 164
- The Dark Energy Survey Collaboration 2005, arXiv:astro-ph/0510346
- van der Wel, A., Bell, E. F., Häussler, B., et al. 2012, *ApJS*, **203**, 24
- van der Wel, A., Franx, M., van Dokkum, P. G., et al. 2014, *ApJ*, **788**, 28
- van Dokkum, P. G., Brammer, G., Fumagalli, M., et al. 2011, *ApJL*, **743**, L15
- van Dokkum, P. G., Nelson, E. J., Franx, M., et al. 2015, *ApJ*, **813**, 23
- Weinmann, S. M., Kauffmann, G., van den Bosch, F. C., et al. 2009, *MNRAS*, **394**, 1213
- Whitaker, K. E., Bezanson, R., van Dokkum, P. G., et al. 2017, *ApJ*, **838**, 19
- Whitaker, K. E., Franx, M., Bezanson, R., et al. 2015, *ApJL*, **811**, L12
- Whitaker, K. E., Labbé, I., van Dokkum, P. G., et al. 2011, *ApJ*, **735**, 86
- Whitaker, K. E., van Dokkum, P. G., Brammer, G., & Franx, M. 2012, *ApJL*, **754**, L29
- Wuyts, S., Förster Schreiber, N. M., Genzel, R., et al. 2012, *ApJ*, **753**, 114